2ND SOUTHERN AFRICAN HYDROGEN AND FUEL CELL CONFERENCE 2025

7-8 APRIL 2025

SOUTHERN SUN ROSEBANK, JOHANNESBURG

Proceedings

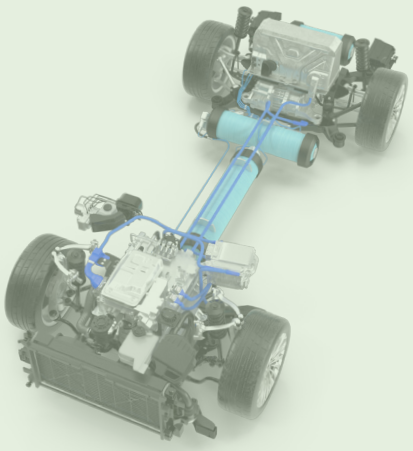

SAIMM
THE SOUTHERN AFRICAN INSTITUTE OF MINING AND METALLURGY
130 Years OF TECHNICAL EXCELLENCE

THE SOUTHERN AFRICAN INSTITUTE OF MINING AND METALLURGY
JOHANNESBURG 2025

2ND Southern African Hydrogen and Fuel Cell Conference 2025

7-8 APRIL 2025

SOUTHERN SUN ROSEBANK, JOHANNESBURG

SAIMM PUBLICATIONS

THE MONOGRAPH SERIES

Ml **Lognormal-De Wijsian Geostatistics for Ore Evaluation**
(2nd ed 1981) D.G. Krige

M2 **An Introduction to Geostatistical Methods of Mineral Evaluation**
(2nd ed 1981) J.-M.M. Rendu

M3 **Principles of Flotation**
(1982) (3rd imp. 1986) Edited by R.P. King

M4 **Increased Underground Extraction of Coal**
(1982) Edited by C.J. Fauconnier and R.W.O. Kersten

M5 **Rock Mechanics in Mining Practice**
(1983) (3rd imp. 1986) Edited by S. Budavari

M6 **Assay and Analytical Practice in the South African Mining Industry**
(1986) W.C. Lenahan and R. de L. Murray-Smith

M7 **The Extractive Metallurgy of Gold in South Africa,**
2 volumes (1987) Edited by G.G Stanley

M8 **Mineral and Metal Extraction — An Overview**
(1994) L.C. Woollacott and R.H. Eric

M9 **Rock Fracture and Rockbursts—an illustrative study**
(1997) Edited by W.D. Ortlepp

THE SPECIAL PUBLICATIONS SERIES

SPI **Proceedings, Underground Transport Symposium**
(1986) Edited by R.C.R. Edgar

SP2 **Backfill in South African Mines (1988)**

SP3 **Treatment and Re-use of Water in the Minerals Industry (1989)**

SP4 **COREX Symposium 1990**
(1990) Edited by H.M.W. Delport and P.J. Holaschke

SP5 **Measurement, Control, and Optimization in Mineral Processing**
(1994) Edited by H.W. Glen

SP6 **Handbook on Hard-rock Strata Control**
(1994) A.J.S. Spearing

SP7 **Rock Engineering for underground coal mining**
(2002) J. Nielen van der Merwe and Bernard J. Madden

SP8 **Second Edition: Rock Engineering for underground coal mining**
(2010) J. Nielen van der Merwe and Bernard J. Madden

SP9 **Theoretical Rock Mechanics for Professional Practice**
(2016) M. Handley

SP10 **Johannesburg and its Holey Mining Heritage 2021**
(2021) T.R. Stacey

SP11 **Mineral and Metal Extraction — An Overview**
(2021) L.C. Woollacott and R.H. Eric

SP12 **The Fall of a Giant: The story of the disintegration of the South African Mining Industry**
(2022/2023) Dr I. Robinsoin

SP13 **COMRO's Legacy: Research and Development of Stoping Mining Machinery and Technologies**
(2023) B. Protheroe

SUPPLEMENT TO THE SAIMM JOURNAL

The Metals and Minerals Industry in South Africa - Part 1 (1989)
Edited by H.W. Glen

THE SYMPOSIUM SERIES

S1 **Mathematical Statistics and Computer Applications in Ore Valuation (1966)**

S2 **Planning Open Pit Mines** (1970) (4th imp.)
Edited by P.W.J. van Rensburg

S3 **Application of Computer Methods in the Mineral Industry** (APCOM 1973) Edited by M.D.G. Salamon

S4 **Infacon 1974** Edited by H.W. Glen

S5 **Proceedings of the 12TH CMMI Congress** 2 volumes (1982)
Edited by H.W. Glen

S6 **Rockbursts and Seismicity in Mines** (1984)
Edited by N.C. Gay and E.H. Wainwright

S7 **The Planning and Operation of Open Pit and Strip Mines** (1986) Edited by J.P. Deetlefs

S8 **GOLD 100: Proceedings of the International Conference on Gold (1986)**
Volume 1: Gold Mining Technology
Edited by H. Wagner and R.P. King
Volume 2: Extractive Metallurgy of Gold
Edited by C.E. Fivaz and R.P. King
Volume 3: Industrial Uses of Gold
Edited by G. Gafner and R.P. King

S9 **APCOM 87: Proceedings of the Twentieth International Symposium on the Application of Computers and Mathematics in the Mineral Industries (1987)**
Volume 1: Mining
Edited by L. Wade, R.W.O. Kersten and J.R. Cutland
Volume 2: Metallurgy
Edited by R.P. King and I.J. Barker
Volume 3: Geostatistics
Edited by I.C. Lemmer, H. Schaum and F.A.G.M. Camisani-Calzolari

S10 **International Deep Mining Conference (1990)**
Volume 1: Innovations in Metallurgical Plant
Edited by G.A. Brown and P. Smith
Application of Materials Engineering in the Mining Industry Edited by B. Metcalfe
Volume 2: Technical Challenges in Deep Level Mining
Edited by D.A.J. Ross-Watt and P.D.K. Robinson

S11 **Infacon 6 (Incorporating Incsac) (1992)**
Edited by H.W. Glen

S12 **Massmin 92**
Edited by H.W. Glen (out of print)

S13 **Minefill 93**
Edited by H.W. Glen

S14 **XVTH CMMI Congress Publications (1994)**
Volume 1: Mining
Edited by H.W. Glen
Volume 2: Metals Technology and Extractive Metallurgy (1994) Edited by H.W. Glen

S15 **Surface Mining 1996**
Edited by H.W. Glen

S16 **Hidden Wealth (1996)**
Edited by H.W. Glen

S17 **Heavy Minerals 1997**
Edited by R.E. Robinson

S18 **The 8TH International Platinum Symposium (1998)**

S19 **Mining in Africa '98**

S20 **Extraction Metallurgy Africa '98**

S21 **Sixth International Symposium for Rock Fragmentation by Blasting (1999)**

S22 **Metallurgy Africa '99**

S23 **Heavy Minerals 1999**
Edited by R.G. Stimson

S24 **Tunnels under Pressure**
Technical Editor T.R. Stacey

S25 **Mine Hoisting 2000**

S26 **Coal–The Future (2000)**

S27 **The Fifth International Symposium on Rockburst and Seismicity in Mines (RaSim 5) (2001)**

S28 **6TH International Symposium on Mine Mechanization and Automation (2001)**

S29 **XIV International Coal Preparation Congress and Exhibition**

S30 **Surface Mining 2002—Modern Developments for the New Millennium**

S31 **IFSA 2002, Industrial Fluidization South Africa**

S31a **APCOM 2003—Application of Computers and Operations Research in the Minerals Industries**

S32 **ISSA/Chamber of Mines Conference—Mines and Quarries: Prevention of Occupational Injury and Disease**

S33 **ISRM—Technology Roadmap for Rock Mechanics**

S34 **Heavy Minerals Conference 2003**

S35 **Safety in Mines Research Institutes (2003)**

S36 **VII International Conference on Molten Slags, Fluxes & Salts (2004)**
Tenth International Ferroalloys Congress INFACONX 2004

S37 **Deep and high stress mining 2004**

S38 **'Platinum adding value' 2004**

S39 **Base Metals—Southern Africa's response to changing global base metals market dynamics 2005**

S40 **Strategic *versus* Tactical approaches in mining 2005**

S41 **Best practices in rock engineering SARES 2005**

S42 **IFSA 2005, Industrial Fluidization South Africa**

S43 **Southern African Pyrometallurgy 2006 International Conference**

S44 **Stability of rock slopes in open pit mining and civil engineering situations**

S45 **'Platinum Surges Ahead' 2006**

S46 **Hydraulic Transport of Solids - Hydrotransport 17 (2007)**

S47 **Fourth Southern African Base Metals Conference 'Africa's base metals resurgence'**

S48 **Heavy Minerals Conference, 2007**

S49 **Cave Mining Conference, 2007**

S50 **International Symposium on Lead and Zinc processing – Lead & Zinc 2008**

S51 **Surface Mining 2008**

S52 **Platinum in transformation 2008**

S53 **IFSA 2008, Industrial Fluidization South Africa**

S54 **Hydrometallurgy Conference 2009**

S55 **Shotcrete for Africa 2009**

S56 **Base Metals Conference 2009**

S57 **Heavy Minerals Conference, 2009**

S58 **Hard Rock Safe—Safety Conference 2009**

S59 **Sampling and Blending 2009**

S60 **World Gold 2009 Conference**

S61 **Physical Beneficiation Conference 2010**

S62 **Second Hardrock Safe—Safety Conference 2010**

S63 **Platinum in Transition 'Boom or Bust' 2010**

S64 **South African Pyrometallurgy 2011 International Conference**

S65 **Minefill 2011 (10TH International Symposium on Mining with Backfill)**

S66 **Base Metals Conference 2011**

S67 **MineSafe 2011 Conference**

S68 **Iron Ore and Manganese Ore Metallurgy 2011**

S69 **Percolation leaching: The status globally and in Southern Africa 2011**

S70 **IFSA 2011, Industrial Fluidization South Africa**

S71 **Southern Hemisphere International Rock Michanics Symposium 2012**

S72 **Platinum Conference 'A catalyst for change' 2012**

S73 **Ferrous 2012—Ferrous and Base Metals Development Network Conference**

S74 **Diamonds - Source to use 2013**

S75 **Sampling and analysis: Best-practice in African mining 2013**

S76 **Base Metals Conference 2013**

S77 **Precious Metals 2013 Conference—The Precious Metals Development Network (PMDN)**

S78 **Physical Beneficiation 2013 Conference**

S79 **21st Century challenges to the southern African coal sector 2014**

S80 **Furnace Tapping Conference 2014**

S81 **Platinum Conference 'Platinum—Metal for the Future' 2014**

S82 **IFSA 2014, Industrial Fluidization South Africa**

S83 **Copper Cobalt Africa 2015**

S84 **The Danie Krige Geostatistical Conference 2015 - Vol. 1**

The Danie Krige Geostatistical Conference 2015 - Vol. 2

S85 **World Gold Conference 2015**

S86 **Slope Stability 2015**

S87 **2nd Annual Young Professionals Conference 2015**

S88 **AMI–Nuclear Materials Development Network 2015**

S89 **MPES–23rd International Symposium on Mine Planning & Equipment Selection 2015**

S90 **Diamonds still Sparkling Conference 2016**

S91 **The SAMREC/SAMVAL Companion Volume Conference 2016**

S92 **New Technology and Innovation in the Minerals Industry Colloquium 2016**

S93 **Theoretical Rock Mechanics for Professional Practice** (Special Publications Series 9) by M. Handley - 2016

S94 **Hydrometallurgy Conference 2016**

S95 **10TH Heavy Minerals Conference 2016**

S96 **MineSafe Conference 2016**

S97 **AMI-Ferrous and Base Metals Development Conference 2016**

S98 **3rd Young Professionals Conference 2017**

S99 **Proximity Detection and Collosion Avoidance Systems in Mining Colloquium 2017**

S100 **6TH Sulphur and Sulphuric Acid Conference 2017**

S101 **Mine Planning Colloquium 2017**

S102 **Chrome Colloquium 2017**

S103 **4TH Mineral Project Valuation Colloquium 2017**

S104 **Water Conference 2017**

S105 **Rapid Underground Mine and Civil Access Engineering 2017**

S106 **MineSafe Conference 2017**

S107 **Uranium 2017 International Conference 2017**

S108 **IFSA 2017–Industrial Fluidization Conference 2017**

S109 **AfriRock 2017–ISRM International Symposium 2017**

S110 **AMI Precious Metals 2017–The Precious Metals Development Network (PMDN) Symposium**

S111 **7TH International Platinum Conference 2017**

S112 **Infacon XV: International Ferro-Alloys Conrgress 2018**

S113 **SOMP–Society of Mining Professors 6TH Regional Conference 2018**

S114 **Digitalization in Mining Conference 2018**

S115 **Diamonds – Source to Use 2018 Conference 2018**

S116 **The 9TH Southern African Base Metals Conference 2018**

S117 **Geometallurgy Conference 2018**

S118 **Mine Safe Technical Conference and Industry Day 2018**

S119 **ASM Conference 2018**

S120 **4TH Young Professionals Conference 2018**

S121 **Furnace Tapping 2018 Conference 2018**

S122 **7TH Sulphur and Sulphuric Acid Conference 2019**

S123 **Mine Planner's Colloquium 2019**

S124 **9TH International Conference on Deep & High Stress Mining 2019**

S125 **New Technology Conference and Trade Show 2019**

S126 **Smart Mining Smart Environment Smart Society Conference 2019**

S127 **The Eleventh International Heavy Minerals Conference 2019**

S128 **Surface Mining Masterclass 2019**

S129 **International Mine Health and Safety Conference 2019**

S130 **Tailings Storage Conference 2020**

S131 **IMPC2020 XXX International Mineral Processing Congress**

S132 **Johannesburg and its Holey Mining Heritage**
(Special Publications Series 10) by T.R. Stacey - 2021

S133 **Mineral and Metal Extraction — An Overview**
(Special Publications Series 11) by L.C. Woollacott and R.H. Eric - 2021

S134 **Diamonds - Source to Use - 2021 Online Conference 2021**

S135 **WorldGold Online Conference 2021**

S136 **APCOM 2021 Minerals Industry4.0-The next digital transformation in mining**

S137 **5TH Young Professionals Online Conference 2021**

S138 **Southern African Rare Earths International Online Conference 2021**

S139 **SAMCODES Conference 2021**

S140 **Global Tailings Standards and Opportunities`For the Mine of the Future Conference 2022**

S141 **The Fall of a Giant: The story of the disintegration of the South African Mining Industry**
(Special Publications Series 12) by I. Robinson - 2022/2023

S142 **Battery Materials Conference 2022**

S143 **32ND SOMP Annual Meeting and Conference 2022**

S144 **SDIMI (Sustainable Development in the Minerals Industry) 10TH International Conference 2022**

S145 **THANOS International Conference 2022**

S146 **Mine Impacted Water Online Conference 2022 (Abstract Book Only)**

S147 **8TH International PGM Conference 2022**

S148 **SANCOT Symposium 2022**

S149 **8TH Sulphur and Sulphuric Acid Conference 2023**

S150 **Southern African Hydrogen and Fuel Cell Conference 2023**

S151 **COMRO's Legacy: Research and Development of Stoping Mining Machinery and Technologies**
(Special Publications Series 13) by B. Protheroe - 2023

S152 **Copper Cobalt Africa in Association with The 10TH Southern African Base Metals Conferenc 2023**

S153 **Digital Transformation in Mining Conference 2023**

S154 **Diamonds Source to Use 2023 Online Conference**

S155 **12TH International Heavy Minerals Conference 2023**

S156 **Geometallurgy Conference 2023**

S157 **Next Generation Tailings Opportunitiy or Risk? Conference 2023**

S158 **6TH Young Professionals Conference 2023**

S159 **Southern African Pyrometallurgy 2024 International Conference**

S160 **The 11TH World Conference of Sampling and Blending 2024**

S161 **SANIRE Symposium 2024**
Technical Applications in Rock Engineering

S162 **2ND International Conference 2024 Southern African Rare Earths**

S163 **2ND Battery Materials Conference 2024**

S164 **Hydrometallurgy Conference 2024**

S165 **Environmental Social Governance Sustainability Conference 2024**

S166 **MineSafe Mine Health and Safety Conference 2024**

S167 **Mintek@90 Conference 2024**

S168 **Mine Closure Conference 2025**

Published by The Southern African Institute of Mining and Metallurgy
Minerals Council South Africa, 7th Floor, Rosebank Towers, 19 Biermann Avenue, Rosebank, 2196
Republic of South Africa

ISBN 978-1-7764673-9-6

The papers in this volume have been for the most part prepared from Word documents supplied by the authors, with additional typesetting and formatting by The Southern African Institute of Mining and Metallurgy.

Organising Committee

The Organising Committee would like to thank the reviewers listed below for the efforts in the reviewing process

O. Barron

H. Moydien

D. Susac

B.S. Xakalashe

Desktop prepared by Camera Press, Johannesburg

FOREWORD

The primary purpose of the 2ND Hydrogen and Fuel Cells conference is the advancement of green hydrogen technologies in Southern Africa and the global community, by highlighting the power of renewable and sustainable technologies and addressing the emerging challenges—through the exploration of hydrogen production, storage and utilization using fuel cells by way of engagement with industry, academia and government. The conference will provide a platform for high level exchange and networking opportunities with various experts in the field. The two-day conference will feature high-level scientific talks and posters, complemented with keynote and plenary presentations on country overviews, status of leading and major players in the Southern African and global arena.

B.S. Xakalashe
Conference Chairperson

Contents

A computational approach to designing high entropy alloys for hydrogen storage

B.S. Ramatsoma[1], E.M. Makhatha[1], D.E.P. Klenam[2], M.O. Bodunrin[2]

[1]University of Johannesburg, South Africa
[2]University of the Witwatersrand, South Africa

The advancement of effective and sustainable hydrogen storage technology is essential for the hydrogen economy. High-entropy alloys (HEAs) have emerged as attractive materials owing to their unique structural characteristics, thermal stability, and customisable hydrogen absorption/desorption kinetics. This paper employs a computational methodology to build HEA-based metal hydrides, employing advanced programs such as HEAPS, Thermo-Calc, and Model MH to optimise alloy composition and microstructure. We examine the interaction between body-centred cubic (BCC) alloys and Laves-phase intermetallics to improve hydrogen storage capacity, phase stability, and performance using a computational approach. Our research offers significant insights into the importance of valence electron concentration (VEC), phase engineering, and thermodynamic modelling in the design of HEAs. These computational improvements facilitate the creation of next-generation hydrogen storage materials, which have substantial implications for fuel cell applications, especially in the transportation and renewable energy sectors.

Keywords: hydrogen storage, high-entropy alloys, metal hydrides, computational modelling, fuel cell applications, clean energy.

INTRODUCTION

High entropy alloys (HEAs) have gained significant attention in hydrogen storage due to their unique ability to efficiently absorb and desorb hydrogen under ambient conditions. Unlike conventional materials, HEAs consists of five or more principal elements in nearly equal proportions, forming complex crystal structures such as body-centred cubic (BCC), face-centered cubic (FCC), and hexagonal close-packed (HCP) phases [1,2]. This structural complexity enhances their stability and mechanical properties, making them attractive candidates for hydrogen storage applications. Their high thermal stability and resistance to phase transformations further ensure long-term performance during hydrogen absorption and desorption cycles [3,4].

One major advantage of HEAs is their adjustable composition, which allows for modifications that improve hydrogen diffusion, increase surface area, and enhance hydrogen uptake and release rates [3,4]. These features contribute to higher hydrogen storage capacity and better efficiency compared to conventional materials. Among HEA structures, BCC alloys are particularly promising due to their large interstitial spaces, which facilitate hydrogen absorption [5]. BCC HEAs such as $Ti_{27.5}V_{27.5}Nb_{20}Cr_{12.5}Mn_{12.5}$, TiZrVHfNb, and $Ti_{28}V_{22}Nb_{27}Cr_{15}Mn_8$ have demonstrated hydrogen storage capacities of 3.38 wt%, 2.7 wt%, and 3.65 wt%, respectively, showing strong potential for practical hydrogen storage applications under varying temperature and pressure conditions [6–8].

Another crucial factor in HEA-based hydrogen storage is storage kinetics, which determine how quickly hydrogen can be absorbed and released. The presence of Laves phases, a type of intermetallic phase found in some HEAs, has been shown to significantly improve these kinetics, making HEAs more suitable for applications requiring rapid hydrogen uptake and release [9,10]. While HEAs present a promising avenue for hydrogen storage, further research is needed to fully understand the mechanisms governing hydrogen interaction with these materials. Ongoing studies are providing valuable insights that can help optimise HEA compositions for next-generation hydrogen storage solutions.

Research into hydrogen storage mechanisms in HEAs is ongoing, with a focus on combining BCC alloys and Laves-phase intermetallic to develop advanced metal hydrides. By optimising composition and microstructure, HEA alloys can achieve high hydrogen storage capacities, fast absorption/desorption kinetics, thermal stability, and long-term durability. This paper explores the development of HEA-based metal hydrides using computational tools like HEAPS, Thermo-Calc, and ModelMH to simulate thermodynamic properties, phase stability, and hydrogen storage performance, guiding the design of novel HEAs with improved capabilities.

Computational Tools

HEAPS

High entropy alloy prediction software (HEAPS) is a computational tool designed to calculate thermodynamic properties of HEAs, including atomic weight, density, specific heat, atomic mismatch, valence electron concentration (VEC), Gibbs free energy, enthalpy, entropy, and possible phases. HEAPS enables single or multiple predictions based on the alloy composition [11]. The design of HEAs relies on thermodynamic calculations and semi-empirical parameters derived from Hume-Rothery rules, considering factors like electronegativity, VEC, and atomic size mismatch. The Ω parameter helps predict phase stability, where $\Omega > 1$ favours solid solution formation, while $\Omega < 1$ stabilises ordered phases. Key equations determine properties such as melting point, enthalpy, entropy, atomic mismatch (δ), and VEC, which influence phase formation [12]. Specifically, VEC < 6.87 favours BCC structures, VEC > 8 favours FCC, and Laves phases form in the range of 4–8. These calculations help optimise HEA compositions for desired structural and functional properties [13–16].

Thermo-calc

Thermo-Calc is a powerful computational tool used in materials science and engineering to predict phase changes, generate phase diagrams, and model material behaviour under different conditions. By leveraging thermodynamic principles, extensive material databases, and advanced simulations, it enables researchers to design and optimise alloys with specific properties while reducing reliance on costly experimental testing [17,18]. In this study, Thermo-Calc was employed using an HEA database to analyse phase transitions and develop HEA metal hydrides optimised for hydrogen storage. The focus was on designing alloys with a BCC structure and varying Laves phases, which play a crucial role in hydrogen absorption and desorption kinetics. By predicting phase stability and transformations, the software helped identify ideal compositions to enhance hydrogen storage capacity, cycle stability, and rapid hydrogen release/absorption rates. This systematic approach accelerates the development of efficient HEA metal hydrides, contributing to advanced hydrogen storage solutions for energy applications.

Model-MH

The pressure-composition-temperature (PCT) diagrams in this study were generated using an open-source thermodynamic model developed by Suilherme Zepon to predict the PCT behaviour of BCC metal hydrides in HEAs [19,20]. This model builds on the foundational work of Sahlberg et al., who pioneered research on BCC HEA metal hydrides, which undergo a phase transformation from BCC to BCT during hydrogenation [21]. The model relies on the alloy's chemical composition and applies a phase equilibrium approach that accounts for multiple phases, including BCC, BCT, and FCC, under para-equilibrium conditions. Using a set of thermodynamic equations, the model calculates enthalpy, entropy, and Gibbs free energy variations, incorporating configurational entropy and the site-blocking effect (SBE), which influences hydrogen occupancy in interstitial sites [20]. This framework enables

accurate predictions of phase stability and transitions under different temperature and pressure conditions, aiding in the design of efficient HEA-based hydrogen storage materials.

Possible Applications
Computational modelling of HEA metal hydrides is essential for optimising their performance in energy applications such as hydrogen storage, fuel cells, and energy storage devices. In hydrogen storage, simulations enhance key properties like absorption/desorption kinetics, thermodynamic stability, and cycling performance by analysing atomic interactions and hydrogen diffusion mechanisms [22]. This improves charging and discharging efficiency while reducing material degradation. Additionally, computational modelling aids in designing HEA-based materials for fuel cells, batteries, and supercapacitors by optimising corrosion resistance, thermal stability, and electrochemical performance [23]. HEAs can enhance catalyst durability in fuel cells, improve ion diffusion and cycle stability in lithium-ion and sodium-ion batteries, and increase thermal conductivity in energy systems [24]. Overall, modelling accelerates HEA material development, advancing efficient and sustainable energy technologies.

Environmental impact
The simulation of HEA metal hydrides has the potential to drive a sustainable hydrogen economy by enhancing hydrogen storage capabilities through high volumetric density and adjustable hydrogen binding strength. This allows for optimised storage conditions, reducing reliance on high pressure or low temperatures. HEA metal hydrides offer superior kinetics, faster absorption/desorption cycles, and improved cycling stability, making them ideal for stationary and mobile hydrogen storage [25]. Their corrosion resistance and thermal stability enhance the lifespan and safety of storage systems while lowering maintenance costs. Additionally, HEAs can be produced using abundant, cost-effective materials, reducing dependence on rare or expensive metals like palladium [4,5,26]. Scalable production methods, such as powder metallurgy and additive manufacturing, further improve efficiency and reduce costs [27]. With greater durability and long-term stability, HEA metal hydrides present a more economical and sustainable alternative to conventional hydrogen storage materials, supporting the transition to a hydrogen-based energy economy.

Limitations
Computational modelling of HEA metal hydrides provides a cost-effective and efficient method for designing alloys and predicting material properties, crucial for advancing hydrogen storage technologies. Tools like Thermo-Calc and Model MH enable researchers to explore diverse alloy compositions and hydrogen interactions without expensive and time-consuming experiments, offering insights into thermodynamic stability, phase transitions, and hydrogen kinetics. However, these models have limitations, as they often simulate ideal conditions that may not fully capture real-world complexities such as impurities, defects, and processing effects. Additionally, data-driven models rely on extensive datasets, which may be incomplete for newer HEA compositions [17,18,20]. To ensure reliability, computational predictions should be validated through experimental testing, refining models for greater accuracy and practical application [17,18,28,29]. Integrating simulations with real-world experimentation enhances the development of scalable, high-performance HEA metal hydrides for hydrogen storage.

METHODOLOGY

Over 200 HEA variations were analysed with the use of HEAPS and seven alloys compositions with BCC and Laves phase were selected due to their hydrogen storage and hydrogen storage kinetics. VEC was a governing parameter, as BCC formations occur at a VEC < 6.87 and Laves phase at VEC 4 – 8 while a VEC of 4-6 was targeted as it produces optimal hydrogen properties. The phase fractions were assessed using Thermo-calc at 25°C and 400°C with the aim to access microstructural stability and hydrogen storage potential. PCT diagrams were simulated with the aid Model MH in which hydrogen storage capacity was assessed.

RESULTS AND DISCUSSION

HEAPS results

HEAPs aided in the development of 7 alloys based on Ti-V-Nb-Cr with a VEC that varies from 5-6. The VEC indicates that the alloys designed from HEAPS meet the criteria for the formation of BCC and Laves phase which have beneficial properties in the hydrogen storage capacity and hydrogen storage kinetics. Ti-V-Nb-Cr system was chosen due to its 3 wt% storage capacity which is higher than other alloy systems [30]. An increase in metal hydride stability is observed with an increase in VEC supported by the enthalpy of formations which states that the more negative the enthalpy the more stable the hydride as seen in Table 1

Table 1. VEC From HEAPS

ALLOY	COMPOSITION	VEC	ΔH^{rc} (kJ·mol^{-1})	S^{xs} (bcc) (J·mol^{-1}·K^{-1})
A	$Ti_{25}V_{25}Nb_{25}Cr_{25}$	5	-6.39	-0.85713
B	$Ti_{32}V_{26}Nb_{16}Cr_{17}Mn_{9}$	5.04	-10.6	-0.7545
C	$Ti_{32}V_{26}Nb_{16}Cr_{17}Fe_{9}$	5.13	-11.23	-0.93084
D	$Ti_{20}V_{20}Nb_{20}Cr_{20}Mn_{20}$	5.23	-15.16	-0.69654
E	$Ti_{20}V_{20}Nb_{20}Cr_{20}Fe_{20}$	5.4	-15.78	-1.0168
F	$Ti_{20}V_{20}Nb_{20}Cr_{20}Fe_{10}Mn_{10}$	5.5	-15.44	-0.86654
G	$Ti_{10}V_{10}Nb_{20}Cr_{20}Fe_{20}Mn_{20}$	6	-16.21	-0.83432

Thermo-Calc results

The phase fractions of seven alloys synthesised using the HEAPS method were analysed, revealing the presence of BCC, HCP, and Laves phases. Elements like Ti, V, Cr, and Nb contribute to BCC formation, while Ti promotes HCP [31–33]. The Laves phases, C14 and C15, are influenced by different elements, with C15 linked to Nb and Cr, while C14 is promoted by Fe, Mn, and Cr. Notably, Mn has a stronger influence on Laves phase formation than Fe and Cr [34,35]. Simulations at 25°C and 400°C indicate that alloys B and D are unstable at room temperature, as predicted by Thermo-Calc. The 25°C condition is relevant for PCT testing, while 400°C provides stable and reliable Thermo-Calc predictions.

The findings support the correlation between increasing VEC and higher Laves phase fractions in most alloys, except for slight deviations in alloys B and E. Alloy E still exhibits a larger Laves phase fraction than alloy B, reinforcing the VEC concept. The ability of specific elements to promote phases, especially Mn's strong influence on Laves phase formation, is highlighted. Since the Laves phase improves hydrogen storage kinetics, its presence is a valuable feature of these HEAs. Overall, Table 2 (confirms that all seven alloys are BCC HEAs, expected to demonstrate excellent hydrogen storage capacity.

Table 2. Phase fraction predicted by thermo-calc HEA database

Sample	Temperature (°C)	BCC (%)	Laves phase (%)	HCP (%)
A	25	54.3	20.7	24.9
	400	68.6	12.5	18.8
B	400	68.5	18.8	12.7
C	25	69.1	8	22.4
	400	42.7	1	16.5
D	400	51.4	47.1	1.5
E	25	33	16.6	0
	400	88.7	11.3	0
F	25	60.1	30.9	9
	400	68.9	31.1	0
G	25	44.5	43.8	0
	400	32.8	67.2	0

Model MH

The simulated PCT diagrams in Figure 1 confirm that all seven HEA alloys exhibit hydrogen storage capacities exceeding 3 wt%, supporting the Ti-V-Nb system as a strong candidate for hydrogen storage applications. Among them, alloys B and C demonstrate the highest storage capacities, reaching approximately 3.5 wt%, though still below the US DOE target of 5.5 wt% [36]. This superior capacity is attributed to their higher Ti content, as Ti has a strong affinity for hydrogen, significantly enhancing the storage properties of the alloys [37].

Ti plays a crucial role in improving hydrogen storage by facilitating structural modifications in the alloy matrix. With its HCP structure, Ti promotes the formation of tetragonal and cubic lattices through lattice misfit and interactions with other elements, leading to enhanced absorption kinetics and overall storage capacity. These structural adaptations optimise hydrogen storage and release, making Ti a key element in the design of efficient HEA metal hydrides [7,38].

A limitation of the model arises in alloy D, where only the PCT curve at room temperature could be simulated, unlike the other alloys, which include higher temperature simulations. This constraint highlights a modelling limitation in predicting hydrogen absorption at elevated temperatures for certain alloys. Nonetheless, the model remains a valuable tool for providing initial insights into hydrogen storage properties, reducing reliance on costly and time-consuming experimental trials. By predicting the performance of various alloy compositions, the model streamlines the alloy design process, identifying promising candidates for further validation.

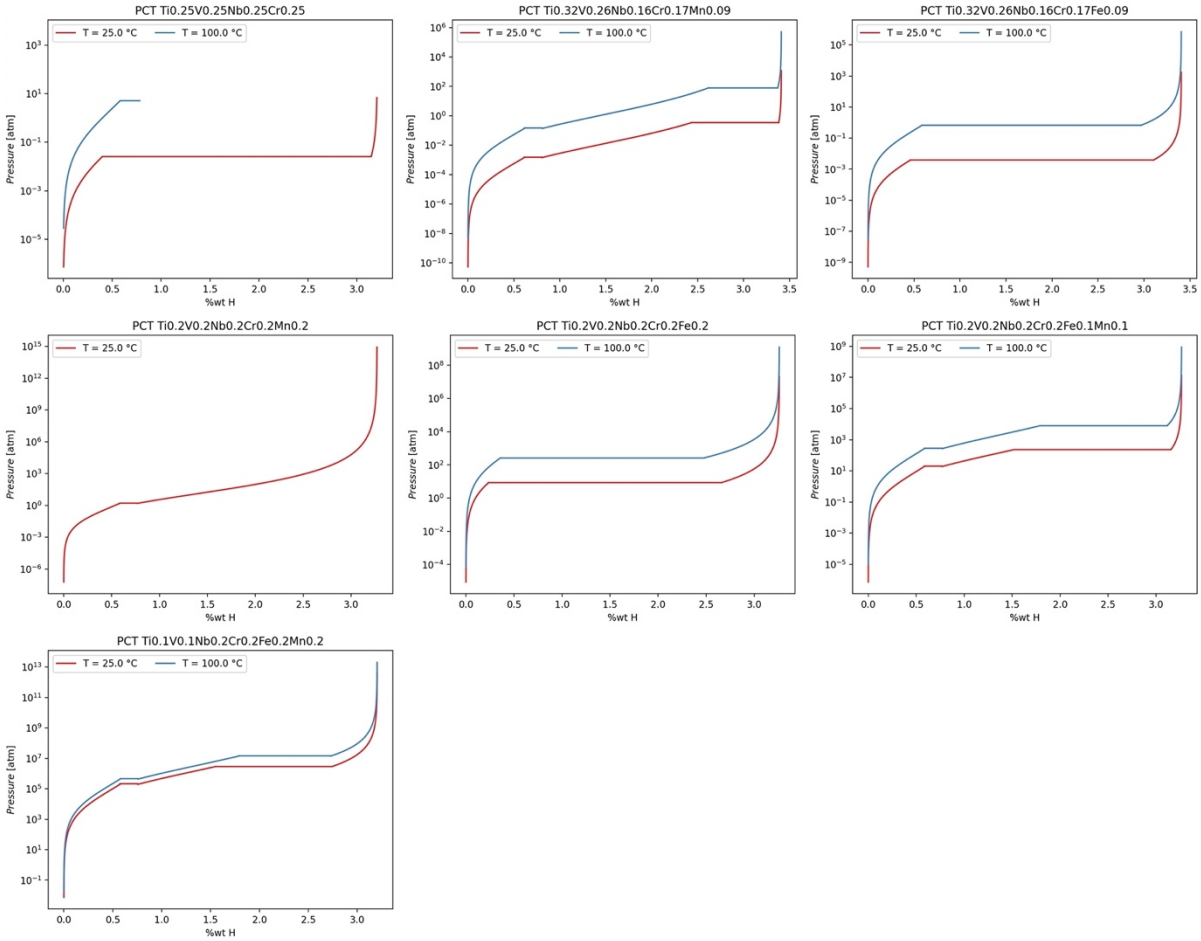

Figure 1. PCT diagrams from Model MH

CONCLUSION

This paper focuses on developing an innovative computational approach for conceptualising HEA metal hydrides for solid-state hydrogen storage. From an initial pool of 200 alloys, seven HEA alloys were simulated using three advanced computational tools which are HEAPS, Thermo-Calc, and an open-source model developed by Zepon. These tools generated detailed PCT diagrams, revealing that the selected alloys exhibit a hydrogen storage capacity exceeding 3 wt% at room temperatures; a high value for HEA metal hydrides. By reducing reliance on traditional trial-and-error methods, this computational approach streamlines the alloy development process, enabling researchers to predict and optimise hydrogen storage properties before experimental validation.

The integration of HEAPS, Thermo-Calc, and Zepon's model allows for efficient simulation and refinement of hydrogen absorption and desorption behaviours, accelerating the advancement of HEA-based hydrogen storage materials. This methodology not only enhances the design of alloys with improved storage capacities but also establishes a framework for future HEA metal hydrides with superior performance characteristics. Ultimately, this study lays the foundation for further research and development in HEA-based hydrogen storage systems, supporting sustainable energy solutions. The computational techniques used can be extended to other HEA compositions, fostering the discovery of novel materials for efficient and reliable hydrogen storage in various energy applications.

REFERENCES

[1] J.W. Yeh, S.K. Chen, S.J. Lin, J.Y. Gan, T.S. Chin, T.T. Shun, C.H. Tsau, S.Y. Chang, Nanostructured high-entropy alloys with multiple principal elements: Novel alloy design concepts and outcomes, Adv Eng Mater 6 (2004). https://doi.org/10.1002/adem.200300567.

[2] B. Cantor, I.T.H. Chang, P. Knight, A.J.B. Vincent, Microstructural development in equiatomic multicomponent alloys, Materials Science and Engineering: A 375–377 (2004). https://doi.org/10.1016/j.msea.2003.10.257.

[3] M. Rhode, A. Wetzel, O. Ozcan, J. Nietzke, T. Richter, D. Schroepfer, Hydrogen diffusion and local Volta potential in high- And medium-entropy alloys, in: IOP Conf Ser Mater Sci Eng, 2020. https://doi.org/10.1088/1757-899X/882/1/012015.

[4] A. Bouzidi, E. Elkaim, V. Nassif, C. Zlotea, Effect of Cr/Mn Addition in TiVNb on Hydrogen Sorption Properties: Thermodynamics and Phase Transition Study, Hydrogen (Switzerland) 5 (2024). https://doi.org/10.3390/hydrogen5010008.

[5] J. Chen, Z. Li, H. Huang, Y. Lv, B. Liu, Y. Li, Y. Wu, J. Yuan, Y. Wang, Superior cycle life of TiZrFeMnCrV high entropy alloy for hydrogen storage, Scr Mater 212 (2022). https://doi.org/10.1016/j.scriptamat.2022.114548.

[6] L. Serrano, M. Moussa, J.Y. Yao, G. Silva, J.L. Bobet, S.F. Santos, K.R. Cardoso, Development of Ti-V-Nb-Cr-Mn high entropy alloys for hydrogen storage, J Alloys Compd 945 (2023). https://doi.org/10.1016/j.jallcom.2023.169289.

[7] J. Hu, J. Zhang, H. Xiao, L. Xie, G. Sun, H. Shen, P. Li, J. Zhang, X. Zu, A first-principles study of hydrogen storage of high entropy alloy TiZrVMoNb, Int J Hydrogen Energy 46 (2021). https://doi.org/10.1016/j.ijhydene.2021.03.200.

[8] B. Cheng, Y. Li, X. Li, H. Ke, L. Wang, T. Cao, D. Wan, B. Wang, Y. Xue, Solid-State Hydrogen Storage Properties of Ti–V–Nb–Cr High-Entropy Alloys and the Associated Effects of Transitional Metals (M = Mn, Fe, Ni), Acta Metallurgica Sinica (English Letters) 36 (2023). https://doi.org/10.1007/s40195-022-01403-9.

[9] P. Edalati, R. Floriano, A. Mohammadi, Y. Li, G. Zepon, H.W. Li, K. Edalati, Reversible room temperature hydrogen storage in high-entropy alloy TiZrCrMnFeNi, Scr Mater 178 (2020). https://doi.org/10.1016/j.scriptamat.2019.12.009.

[10] X. Ma, X. Ding, R. Chen, X. Gao, Y. Su, H. Cui, Enhanced hydrogen storage properties of ZrTiVAl1−xFex high-entropy alloys by modifying the Fe content, RSC Adv 12 (2022). https://doi.org/10.1039/d2ra01064j.

[11] P. Martin, C.E. Madrid-Cortes, C. Cáceres, N. Araya, C. Aguilar, J.M. Cabrera, HEAPS: A user-friendly tool for the design and exploration of high-entropy alloys based on semi-empirical parameters, Comput Phys Commun 278 (2022). https://doi.org/10.1016/j.cpc.2022.108398.

[12] X. Yang, Y. Zhang, Prediction of high-entropy stabilized solid-solution in multi-component alloys, Mater Chem Phys 132 (2012). https://doi.org/10.1016/j.matchemphys.2011.11.021.

[13] A. Amiri, R. Shahbazian-Yassar, Recent progress of high-entropy materials for energy storage and conversion, J Mater Chem A Mater 9 (2021). https://doi.org/10.1039/d0ta09578h.

[14] George E.P, Raabe D, Ritchie R.O, High-entropy alloys, Nat Rev Mater 4 (2019) 515–534.

[15] S. Guo, C. Ng, J. Lu, C.T. Liu, Effect of valence electron concentration on stability of fcc or bcc phase in high entropy alloys, in: J Appl Phys, 2011. https://doi.org/10.1063/1.3587228.

[16] Z.S. Nong, J.C. Zhu, R. Da Zhao, Prediction of structure and elastic properties of AlCrFeNiTi system high entropy alloys, Intermetallics (Barking) 86 (2017). https://doi.org/10.1016/j.intermet.2017.03.014.

[17] J. Ågren, CALPHAD - An Approach to Predict Microstructural Stability, in: Encyclopedia of Materials: Metals and Alloys, 2021. https://doi.org/10.1016/B978-0-12-819726-4.00042-9.

[18] J.O. Andersson, T. Helander, L. Höglund, P. Shi, B. Sundman, Thermo-Calc & DICTRA, computational tools for materials science, CALPHAD 26 (2002). https://doi.org/10.1016/S0364-5916(02)00037-8.

[19] G. Zepon, B.H. Silva, C. Zlotea, W.J. Botta, Y. Champion, Thermodynamic modelling of hydrogen-multicomponent alloy systems: Calculating pressure-composition-temperature diagrams, Acta Mater 215 (2021). https://doi.org/10.1016/j.actamat.2021.117070.

[20] O.A. Pedroso, W.J. Botta, G. Zepon, An open-source code to calculate pressure-composition-temperature diagrams of multicomponent alloys for hydrogen storage, Int J Hydrogen Energy 47 (2022). https://doi.org/10.1016/j.ijhydene.2022.07.179.

[21] M. Sahlberg, D. Karlsson, C. Zlotea, U. Jansson, Superior hydrogen storage in high entropy alloys, Sci Rep 6 (2016). https://doi.org/10.1038/srep36770.

[22] S. Tiwari, P. Sharma, Design of metal hydride reactor with embedded helical coil using optimization methods, Engineering Research Express 3 (2021). https://doi.org/10.1088/2631-8695/abf9e5.

[23] B. Cheng, L. Kong, H. Cai, Y. Li, Y. Zhao, D. Wan, Y. Xue, Exploring microstructure variations and hydrogen storage characteristics in TiVNbCrNi high-entropy alloys with different Ni incorporation, Int J Hydrogen Energy 72 (2024) 29–40. https://doi.org/10.1016/J.IJHYDENE.2024.05.317.

[24] Y. Wei, X. Liu, R. Yao, J. Qian, Y. Yin, D. Li, Y. Chen, Embedding the high entropy alloy nanoparticles into carbon matrix toward high performance Li-ion batteries, J Alloys Compd 938 (2023). https://doi.org/10.1016/j.jallcom.2022.168610.

[25] T.R. Somo, M. V. Lototskyy, V.A. Yartys, M.W. Davids, S.N. Nyamsi, Hydrogen storage behaviours of high entropy alloys: A Review, J Energy Storage 73 (2023). https://doi.org/10.1016/j.est.2023.108969.

[26] T. Qureshi, M.M. Khan, H.S. Pali, The future of hydrogen economy: Role of high entropy alloys in hydrogen storage, J Alloys Compd 1004 (2024) 175668. https://doi.org/10.1016/J.JALLCOM.2024.175668.

[27] T. Ron, A. Leon, V. Popov, E. Strokin, D. Eliezer, A. Shirizly, E. Aghion, Synthesis of Refractory High-Entropy Alloy WTaMoNbV by Powder Bed Fusion Process Using Mixed Elemental Alloying Powder, Materials 15 (2022). https://doi.org/10.3390/ma15124043.

[28] Y. Zeng, M. Man, C.K. Ng, D. Wuu, J.J. Lee, F. Wei, P. Wang, K. Bai, D.C. Cheh Tan, Y.W. Zhang, Machine learning-based inverse design for single-phase high entropy alloys, APL Mater 10 (2022). https://doi.org/10.1063/5.0109491.

[29] E. Halpren, X. Yao, Z.W. Chen, C.V. Singh, Machine learning assisted design of BCC high entropy alloys for room temperature hydrogen storage, Acta Mater 270 (2024) 119841. https://doi.org/10.1016/J.ACTAMAT.2024.119841.

[30] B. Cheng, L. Kong, H. Cai, Y. Li, Y. Zhao, D. Wan, Y. Xue, Exploring microstructure variations and hydrogen storage characteristics in TiVNbCrNi high-entropy alloys with different Ni incorporation, Int J Hydrogen Energy 72 (2024) 29–40. https://doi.org/10.1016/J.IJHYDENE.2024.05.317.

[31] N. Pineda-Romero, L. Perrière, E. Elkaim, C. Zlotea, Advancing our understanding of the effect of Al/Mo substitution in the TiVNb alloy on the hydrogen storage properties, J Alloys Compd 1005 (2024) 176255. https://doi.org/10.1016/J.JALLCOM.2024.176255.

[32] S.A. Lushnikov, S.S. Agafonov, Structure of a Hydride Based on TiZrHfMoTa High-Entropy Alloy, Inorganic Materials 59 (2023). https://doi.org/10.1134/S0020168523080113.

[33] A. Bouzidi, L. Laversenne, G. Zepon, G. Vaughan, V. Nassif, C. Zlotea, Hydrogen Sorption Properties of a Novel Refractory Ti-V-Zr-Nb-Mo High Entropy Alloy, Hydrogen (Switzerland) 2 (2021). https://doi.org/10.3390/hydrogen2040022.

[34] X. Ma, X. Ding, R. Chen, W. Cao, Q. Song, Study on hydrogen storage property of (ZrTiVFe)xAly high-entropy alloys by modifying Al content, Int J Hydrogen Energy 47 (2022) 8409–8418. https://doi.org/10.1016/J.IJHYDENE.2021.12.172.

[35] G. Li, Y. Li, J. Liang, Z. Wen, T. Zhang, X. Ding, Y. Qu, Influence of C14 Laves phase and Zr-rich phase interactions on the hydrogen storage properties of Ti32.5V27.5Zr7.5Nb32.5 high entropy hydrogen storage alloy, Intermetallics (Barking) 168 (2024) 108239. https://doi.org/10.1016/J.INTERMET.2024.108239.

[36] Q. Ain, H.T. Naeem, M. Ali, J. Munir, Z. Bibi, H.M. Ghaithan, A.A.A. Ahmed, S.M.H. Qaid, A precise prediction of structure stability and hydrogen storage capability of KCdH3 perovskite hydride using density functional theory calculations, J Energy Storage 100 (2024) 113734. https://doi.org/10.1016/J.EST.2024.113734.

[37] C. Zlotea, M.A. Sow, G. Ek, J.P. Couzinié, L. Perrière, I. Guillot, J. Bourgon, K.T. Møller, T.R. Jensen, E. Akiba, M. Sahlberg, Hydrogen sorption in TiZrNbHfTa high entropy alloy, J Alloys Compd 775 (2019). https://doi.org/10.1016/j.jallcom.2018.10.108.

[38] J. Hu, J. Zhang, H. Xiao, L. Xie, H. Shen, P. Li, J. Zhang, H. Gong, X. Zu, A Density Functional Theory Study of the Hydrogen Absorption in High Entropy Alloy TiZrHfMoNb, Inorg Chem 59 (2020). https://doi.org/10.1021/acs.inorgchem.0c00989.

Ramatsoma Bongani Seeke

Assistant Lecturer
University of Johannesburg

Mr Ramatsoma BS is an Assistant Lecturer in the Department of Metallurgy at the University of Johannesburg, specializing in materials science and hydrogen storage technologies. Currently pursuing a PhD, their research focuses on high entropy alloy (HEA) metal hydrides as a novel solution for hydrogen storage. By exploring the thermodynamic, structural, and kinetic properties of these materials, He aims to enhance their performance in terms of storage density, reversibility, and stability, contributing to the advancement of sustainable hydrogen storage technologies for clean energy applications.

As an educator, Mr Ramatsoma teaches undergraduate courses in materials science at UJ. They are dedicated to mentoring the next generation of engineers and materials scientists by blending theoretical knowledge with practical, hands-on learning. Through their work, Mr. Ramatsoma is helping to aims to development of efficient, sustainable energy solutions and contribute to the global transition to clean energy.

Optimisation of metal hydride tanks for hydrogen storage through heat and mass transfer modelling

B.L. Hem, A. Kolesnikov

Tshwane University of Technology, South Africa

The research for this paper on metal hydride (MH) tanks was done to identify design parameters for optimization of hydrogen storage. The main objective was to develop an equation that could be used to calculate the desired hydrogen charge rate and discharge rate as a function of the reactor's dimensions, inlet conditions, and boundary conditions. This was accomplished with the aid of a semi-empirical formula that was created from a collection of experimental data. COMSOL software was used to simulate the heat and mass transfer in the hydrogen storage tank and produce experimental data. Simulations for several MH tank geometries with various boundary conditions were performed, and the charge/discharge rates were predicted, as well as the time to achieve 90% of the maximum H_2 capacity. A two-dimensional model of heat and mass transfer in a MH tank for hydrogen storage was developed as a set of partial differential equations. These partial differential equations describe spatial (in space) and temporal (in time) variations of temperature, pressure, velocity, and hydrogen concentration in the volume of the tank and MH particles. Analytical solutions are not possible due to the strong nonlinearity of these equations; hence numerical methods must be used; therefore, COMSOL software was selected to perform simulations. The model was used to run independent simulations for absorption and desorption for various boundary conditions. Via simulations, the effects of the tank parameters such as length, number of plates and spacing between plates inside the MH tank in the hydrogen absorption processes employing $LaNi_5$ alloy were investigated.

INTRODUCTION

Hydrogen and energy have a long history of working together. Engineers were captivated by the early demonstrations of fuel cells and water electrolysis in the 1800s, and since then hydrogen was used to power the first internal combustion engines about 200 years ago (Birol, 2019). The usage of fossil fuels has an impact on a number of issues, such as global warming and pollution. A long-term answer to the problems is to switch to renewable energy sources from traditional fossil fuels (Bao *et al.*, 2013). Among the several substitutes, hydrogen fuel holds the most promise for supply diversification, reduced pollution, and lowered greenhouse gas emissions (Mellouli *et al*., 2010). Making hydrogen economically viable in a secure condition with the necessary storage capacity needs is one of the challenges that businesses face. The adsorption of hydrogen in metal hydride (MH) tanks has been found by researchers from all over the world to be a potential answer to the issue of storing hydrogen. The use of MH tanks as hydrogen storage tanks has attracted the attention of researchers from around the globe as a potential method for storing hydrogen. A cylindrical tank that contains metal hydride powder is known as a MH tank (bed). Because metal alloys and hydrogen can react to form MHs, which can then be solidified; MHs offer a safe and effective alternative for storing hydrogen (Afzal and Sharma, 2018).

Theoretical models were also created to better examine the transport mechanisms. Investigational tests on the absorption/desorption processes of hydrogen in La-Ni formed MH beds were conducted (Jiao *et al.*, 2012). In order to assess how well-powdered cylindrical MH beds applied hydrogen gas, a 3D numerical heat-and-mass transfer model was developed (Satya Sekhar *et al*., 2015).

According to a study on hydrogen charge and discharge processes presented both experimentally and numerically to comprehend the process and parameters that should be changed to obtain a desired metal hydride tank, the amount of hydrogen that can be charged or discharged is dependent on temperature and pressure, among other factors (Camara and Attila, 2015). The design of important elements in this study, like the volume inside the tank and the plate's diameter, is crucial.

Problem Statement

The parameter set of fins inside the MH tank for hydrogen storage is one of the issues designers experiences with this method of hydrogen storage. The solutions of heat and mass transfer balance equations are a part of the design of a thermal management of fins for hydrogen adsorption/desorption in the MH bed. The temperature, pressure, velocity, hydrogen concentration in the tank volume, and MH particles must all be described by these partial differential equations in terms of both spatial and temporal changes.

Objective

The major goal is to simulate how operating parameters [such as volume, length, and the distance between plates (fins) inside the tank] influence how an MH tank for hydrogen storage operates. COMSOL software will be used to solve mathematical equations for hydrogen absorption in order to forecast charging hydrogen flow rates.

Methodology

Extensive research is required to ensure that the storage is both commercially viable and used in a secure manner with the required storage capacity. The choice of specific design parameters is one of the crucial components of an MH tank. In a mathematical model of hydrogen absorption and desorption rate, the parameters include the sizes of heat-conducting components found inside the MH tank. These specifications cover the spacing between the plates, the size of the plates, and the recommended number of plates inside the tank, based on its capacity. Simulating the impact of various parameters on the performance of an MH tank used to store hydrogen is the paper's research goal. In particular: to anticipate charging/discharging hydrogen flow rates, mathematical equations for absorption and desorption of hydrogen will be solved using COMSOL software, and the criterion equation will be produced based on dimensional analysis.

The following assumptions were made for the modelled MH tank as storage of hydrogen (Satya Sekhar *et al*., 2015; Mohammadshahi *et al*., 2016) :

a. Since the pressure within the bed is moderate, hydrogen is treated as an ideal gas.
b. The temperature of the solid and the gas are the same (local thermal equilibrium).
c. Radioactive heat transfer has a negligible effect. This assumption holds for all hydride-forming alloys that operate at temperatures considerably below100℃.
d. There is no heat loss or gain to/from the environment because only the heat transfers between the MH and the Heat Transfer Fluid (HTF) is evaluated.
e. The temperature of both the gas and the solid is the same (local thermal equilibrium).
f. Prior to the absorption, it is assumed that 10% of hydrogen is present in the tank.
g. Assumed dimensions of the tank are as follow: Fin height 5 mm, Fin number 60, Gap height 4 mm, and MH container length Fin numbers *(Fin height + Fin gap) = 304 mm

In this investigation, a reactor containing $LaNi_5$ was employed. Due to the symmetrical design, the computational domain can be constrained to two dimensions with an axis boundary. Hydrogen gas is injected from the input during the charging process and passes through the void zone into the porous MH bed. Following the procedure, the reaction causes the particles in the porous zone to absorb hydrogen:

$$LaNi_5 + 3.25H_2 \leftrightarrow LaNi_5H_{6.5} \cdots\cdots\cdots\cdots\cdots (1)$$

The domain is split into two halves after that. The first domain stands in for the packed bed, and the second domain represents the walls of the storage tank. The bigger porous area, which is also the site of the reaction, holds the metal.

Source terms and governing equations

The governing equations and source terms within the MH tank for storage of hydrogen for heat and mass transfer and chemical reaction are given in detail below [7, 2]:

Hydrogen mass balance equation

The hydrogen mass balance is expressed using the continuity equation as

$$\frac{\partial(\varepsilon\rho_g)}{\partial t} + \nabla(\rho_g \overrightarrow{U_g}) = -\dot{m}; \ldots\ldots\ldots\ldots\ldots\ldots\ldots\ldots\ldots\ldots\ldots\ldots\ldots\ldots (2)$$

Where$-\dot{m}$ is the mass flow given in equation 2 and $\overrightarrow{U_g}$is the velocity of hydrogen inside the hydride bed, which is calculated by using Darcy's law given in equation (3). Density for hydrogen mass balance is predicted using ideal gas law equation which is given in equation (4):

$$\overrightarrow{U_g} = -\left(\frac{k}{\mu_g}\right)\nabla P \ldots\ldots\ldots\ldots\ldots\ldots\ldots\ldots\ldots\ldots\ldots\ldots\ldots\ldots (3)$$

Where K is the permeability of the MH bed (m^2) and μ_g is the dynamic viscosity of hydrogen gas.

$$\rho_g = \frac{P_g M_{H_2}}{R_U T} \ldots\ldots\ldots\ldots\ldots\ldots\ldots\ldots\ldots\ldots\ldots\ldots\ldots\ldots (4)$$

WhereP_g is defined as the pressure of the gas (hydrogen), M_{H_2} Molar mass of hydrogen, R_U universal gas law and T temperature of hydrogen.

Mass flow equation

The rate of the mass of hydrogen absorbed by the metal hydride, $\dot{m}$, per unit time and unit volume is given by:

$$\dot{m} = C_a e^{\left(-\frac{E_a}{R_U T}\right) ln\left(\frac{P_g}{P_{eq}}\right)(\rho_{t=0}-\rho_t)} \ldots\ldots\ldots\ldots\ldots\ldots\ldots\ldots\ldots\ldots\ldots (5)$$

Where $C_a$is the absorption rate constant (s−1), $E_a(J(molH_2)^{-1})$ is the absorption activation energy,$p_{eq}$is the hydrogen absorption equilibrium pressure, where ρ values relate to the density of the solid at $t = 0$ (non-hydrogenated) and at any given time (partially hydrogenated, t) during the absorption process. It's also worth noting that because p_{eq} is an absolute pressure, P_g must be one as well.

Equilibrium Pressure

The direction of the chemical reaction is specified by the equilibrium pressure. The reaction progresses to the right to generate an MH if the hydrogen gas pressure is higher than the equilibrium pressure. When the gas pressure falls below the equilibrium pressure, hydrogen is released, and the metal reverts to its original condition. The temperature affects the equilibrium pressure. It rises as the temperature rises and decreases as the temperature falls. The equilibrium pressure is given in equation (6):
The reactor is at equilibrium concerning the hydrogen gas, initially. Then, the equilibrium pressure, P_{eq} (bar) is calculated using the van't Hoff equation

$$P_{eq} = e^{\left\{\frac{\Delta H}{R_U T} - \frac{\Delta S}{R_U} + (\varphi \pm \varphi_O) tan\left[\pi\left(\frac{X}{X_f} - \frac{1}{2}\right)\right] \pm \frac{\beta}{2}\right\}} \ldots\ldots\ldots\ldots\ldots\ldots\ldots\ldots\ldots\ldots\ldots (6)$$

Where ΔH and ΔS are reaction enthalpy and entropy, respectively; φ and $\varphi_0$are the slope factors, and β is the hysteresis factor; X and $X_f$represent the definite and final hydrogen concentrations, respectively

Momentum balance

Momentum equation the combination of mass and Darcy's law velocity is given in equation (7) below:

$$\frac{\partial(\varepsilon\rho_g)}{\partial t} + \nabla\left(-\rho_g\left(\frac{k}{\mu_g}\right)\nabla P_g\right) = 0 \cdots\cdots\cdots\cdots\cdots\cdots\cdots\cdots (7)$$

Where K is defined as permeability and ε is related by the equation:

$$K = C_k \times d_p^2\left(\frac{\varepsilon}{1-\varepsilon}\right)^2 \cdots\cdots\cdots\cdots\cdots\cdots\cdots\cdots (8)$$

Where MH particles are represented by d_p and $C_k = 2.37 \times 10^{-3}$ as a constant.

Energy equation

Assuming thermal equilibrium between the hydride bed and hydrogen, a combined energy equation is considered instead of separate equations for both solid and gas phases:

$$\left(\rho C_p\right)_e \frac{\varphi T}{\varphi t} + \left(\rho_g C_{pg}\right)\vec{U}.\nabla T = K_e\nabla^2 T + Q \cdots\cdots\cdots\cdots\cdots\cdots\cdots\cdots\cdots (9)$$

Q is the source term is given by

$$Q = \dot{m}\left[\frac{\Delta H}{M_g}\right] \cdots\cdots\cdots\cdots\cdots\cdots\cdots\cdots\cdots\cdots\cdots\cdots\cdots\cdots\cdots\cdots (10)$$

In the energy equation, equivalent heat capacity can be expressed as:

$$\left(\rho C_p\right)_e = \left(\varepsilon\rho C_p\right)_g + \left((1-\epsilon)\rho C_p\right)_m \cdots\cdots\cdots\cdots\cdots\cdots\cdots\cdots\cdots\cdots (11)$$

Finally, the effective thermal conductivity is given by:

$$k_e = \epsilon k_g + (1-\varepsilon)k_m \cdots\cdots\cdots\cdots\cdots\cdots\cdots\cdots\cdots\cdots\cdots\cdots\cdots\cdots\cdots (12)$$

The ideal gas equation used to determine gas density is as follows:

$$\rho_g = \frac{P_g M_{H_2}}{R_U T} \cdots\cdots\cdots\cdots\cdots\cdots\cdots\cdots\cdots\cdots\cdots\cdots\cdots\cdots\cdots (13)$$

Initial and boundary conditions

Initially, the fraction, X/X_f of reacted MH is assumed to be uniform and equal to 0.1. Also, the temperature in the reactor is assumed to be uniform.

Initial conditions

$$P_g = P_s; T_m = T_m; T_f = T_m; X = X_m = 0.1X_f \cdots\cdots\cdots\cdots\cdots\cdots (14)$$

Boundary conditions

The outer boundary of the MH tank (for cases I and II) is assumed to be adiabatic:

$$\frac{\partial T(r_o)}{\partial r} = 0 \cdots\cdots\cdots\cdots\cdots\cdots\cdots\cdots\cdots\cdots\cdots\cdots\cdots\cdots\cdots\cdots\cdots\cdots\cdots\cdots (15)$$

The heat transfer fluid flows through the heat exchanger inside/outside the reactor bed and convective boundary condition is given by:

$$-k_e \frac{\partial T}{\partial r} = U(T - T_0); \dots\dots\dots\dots\dots\dots\dots\dots\dots\dots\dots\dots\dots\dots\dots\dots\dots.. (16)$$

Where U is the overall heat transfer coefficient, T and T_0 are the temperature of the MH and the average temperature of HTF, respectively. Where U is the overall heat transfer coefficient, T and T_0 are the temperatures of the MH.

Results

Temperature evaluation

The temperature evolution is shown in Figures 1 and 2 for various fin heights, gap height, and number of fin parameter values. The temperature quickly rises from its original value before dropping to its equilibrium value. This is primarily caused by the quick reaction rate of hydrogen absorption, which is accelerated by the presence of void spaces. The simulation displays a sharp initial temperature increase, demonstrating that the rate of the hydrogen absorption process is rapid initially and that the subsequent immediate release of heat exceeds the rate of heat removal due to heat convection with outside air. The temperature then begins to stabilize.

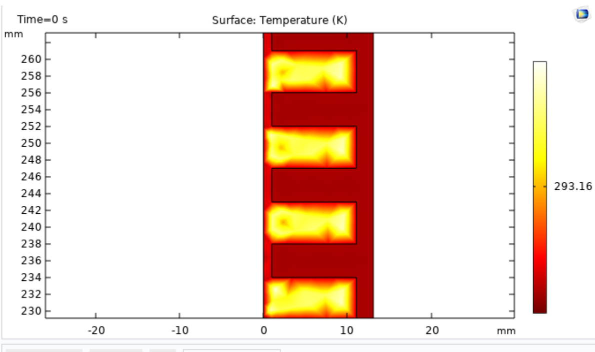

Figure 1. 4 mm fin gap height, temperature surface.

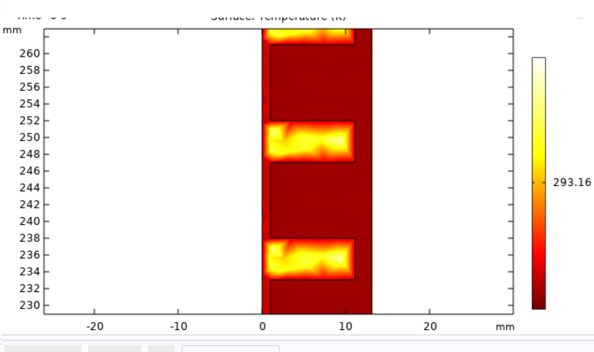

Figure 2. 9 mm fin gap height, temperature surface.

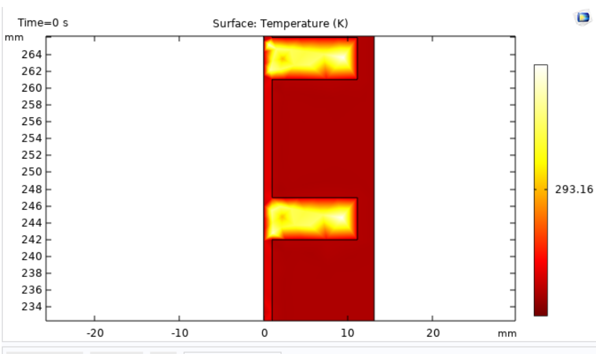

Figure 3. 14 mm fin gap height, temperature surface.

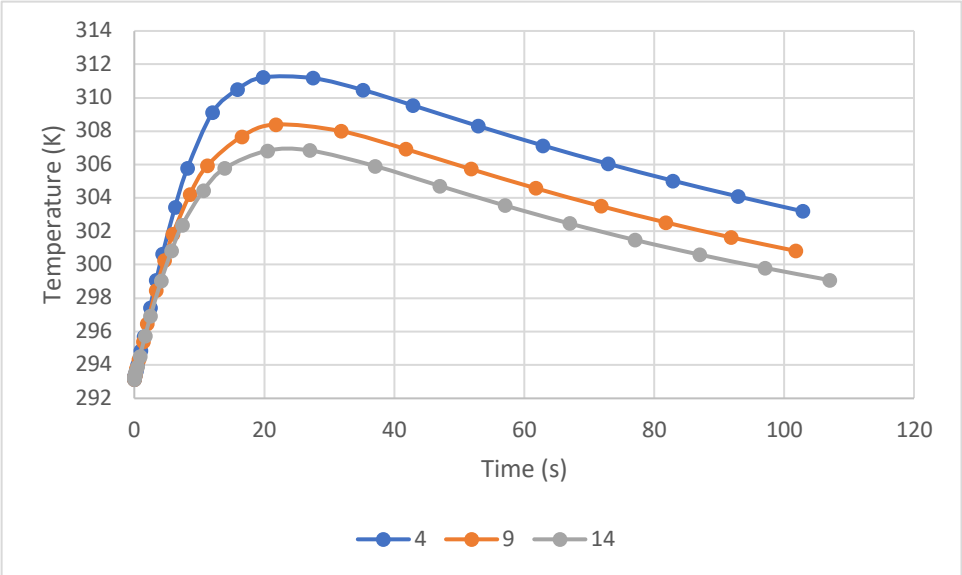

Figure 4. Temperature assessment for three sets of fin gap height parameters (4 mm, 9 mm and 14 mm) in MH storage tank.

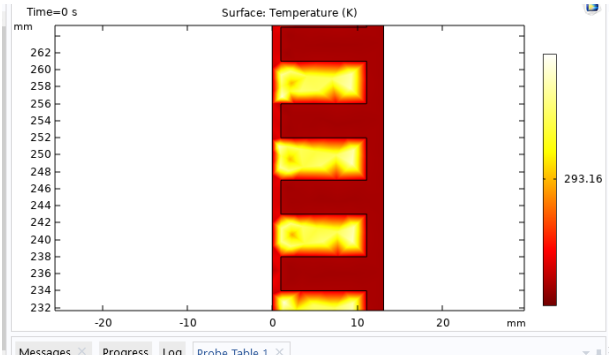

Figure 5. Temperature surface for 40 fins evaluation.

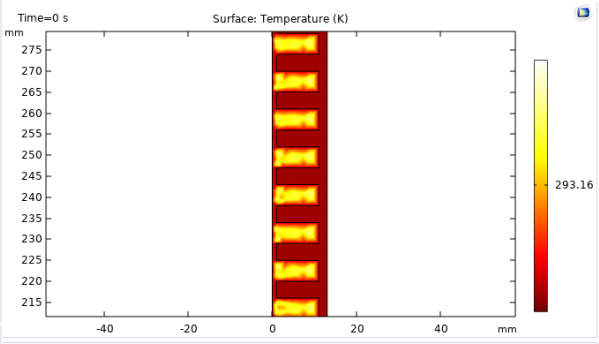

Figure 6. Temperature surface for 80 fins evaluation.

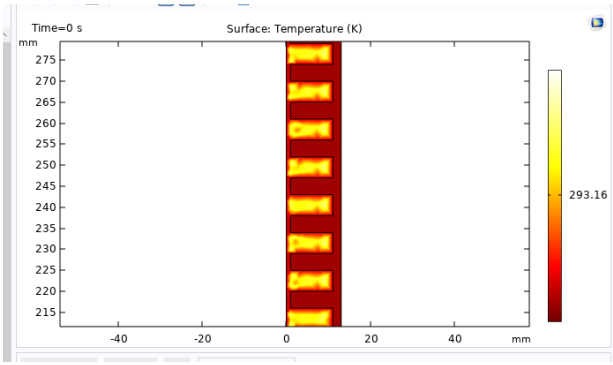

Figure 7. Temperature surface for 120 fins evaluation.

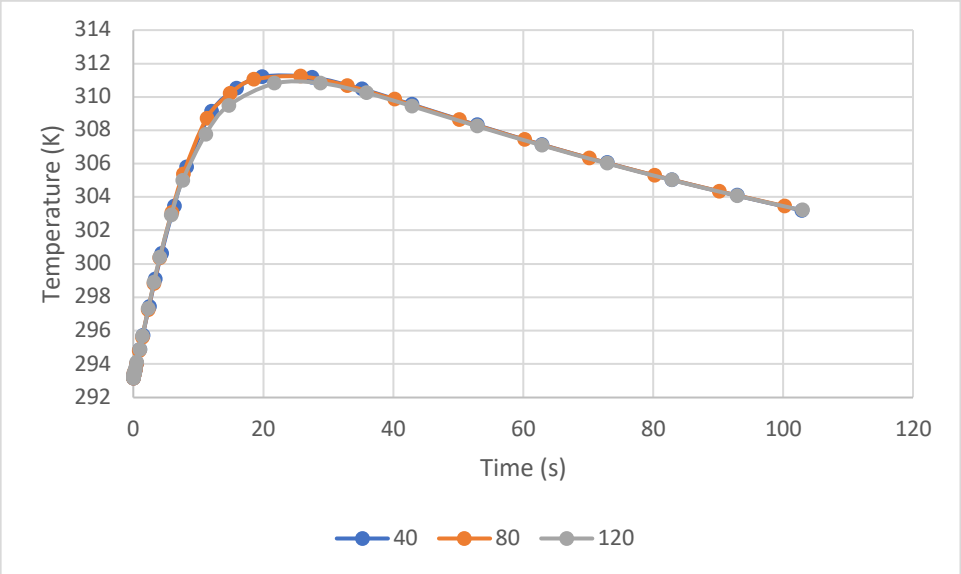

Figure 8. Different fin numbers to evaluate the performance of MH tank as storage of hydrogen.

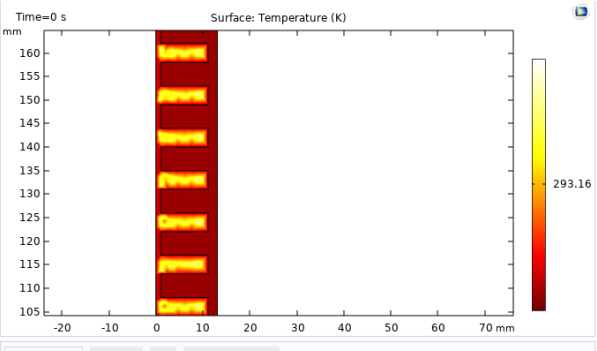

Figure 9. 4 mm fin thickness evaluation. in temperature surface

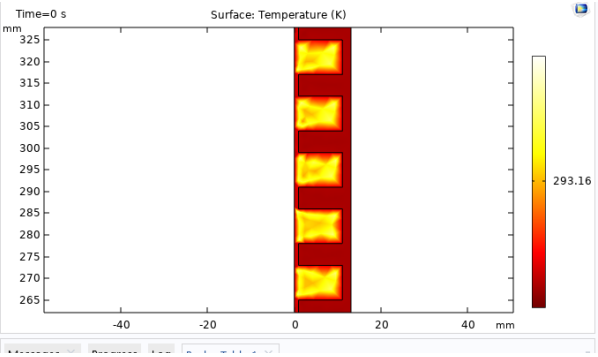

Figure 1. 8 mm fin thickness evaluation in temperature surface.

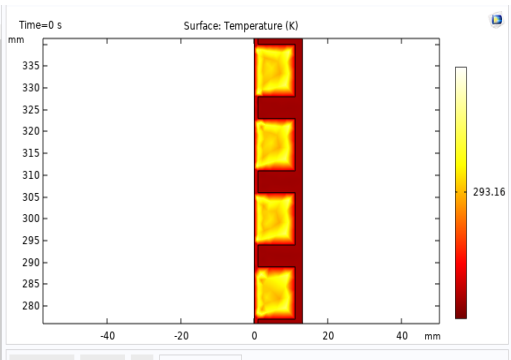

Figure 11. 12 mm of fin thickness evaluation in temperature surface.

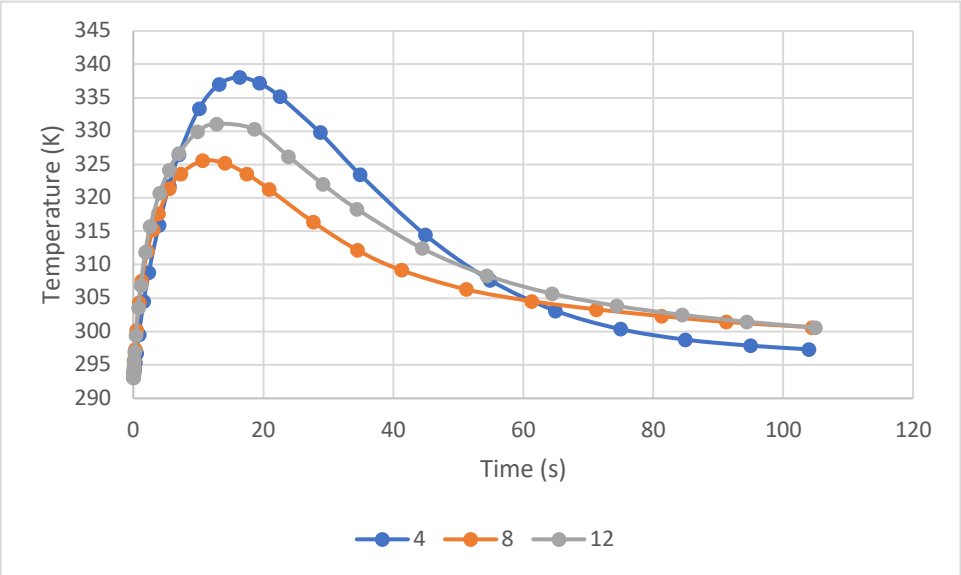

Figure 12. Different fin thickness to evaluate the performance of MH tank as storage of hydrogen.

DISCUSSION

Fin gap height

According to the numbers above, fin gap height affects how temperatures behave. According to (Brendan *et al.*, 2006), the rate at which heat can be transported to the reaction zone has a significant impact on how quickly hydrogen can be taken from an MH tank. According to equation (3), mass conservation and the magnitude of the hydrogen gas velocity in the porous metal vessel is inversely related to the speed of the hydrogen absorption reaction. Because of the first quick hydrogen absorption reaction, it is clear that hydrogen gas speeds are initially high and gradually decrease over time due to the reaction rate slowing down.

Figures 1, 2, and 3 show how the height between fins affects the temperature surface. At 9 mm, the surface temperature rises, causing hydrogen to be absorbed quickly. And when the distance between the fins is between 4 mm and 14 mm, the temperature surfaces drop because the fins' bigger gap and smaller gap produce more room within the MH tank and even smaller space causes hydrogen to be absorbed more slowly than it would otherwise.

These graphics are shown in Figure 4, where it can be seen that this parameter, at 9 mm in height, best represents quick absorption when compared to other parameters.

Number of fins

The temperature surface of fin number evaluation is shown in Figures 5, 6, and 7. Another method for improving heat transfer efficiency in an MH tank used to store hydrogen is the number of fins inside the tank. The results indicate that the number of fins has a significant influence in the design expectations and improves hydrogen storage performance in MH tanks, as shown by the figures for the number of fins in Figures 5, 6, and 7. This can be shown by changing the fin count and observing how the temperature changes behave.

When the number of fins is changed to 80, as shown in Figure 6, it can be seen that the temperature rises, causing the absorption of hydrogen to be faster. However, when the number of fins is lower or higher (40 or 120), the temperature and hydrogen absorption appear to be slower than when the number of fins is 80. The findings of the simulation are used in Figure 8 to illustrate this.

Fin thickness

Figures 9, 10, and 11 display the temperature evaluations for different configurations of fin gaps used to hold hydrogen in MH tanks. One of the most crucial design factors are the fin thickness parameters since they affect the cooling temperature values and heat transfer rates for the MH tanks. The findings in Figures 12 show that a MH tank used to hold hydrogen cools down more quickly at parameter 4 mm than it does at other values, which is supported by a faster transfer rate. This can be explained by the fact that the conduction path is relatively short for thinner beds.

CONCLUSION

Mathematical models for hydrogen absorption and desorption were developed and solved using COMSOL software in order to predict charging hydrogen flow rates. To attain 90% of the maximum H2 capacity, a 2D symmetrical model was utilized to simulate a variety of MH tank shapes with different boundary conditions.

Charging and discharging rate: Applying initial assumption conditions and boundary conditions, absorption simulation was performed using the absorption formulas from equations 3 to 16. Fin height 5 mm, fin spacing 4 mm, fin numbers 60, and fin hole 2 mm were among the geometric fin parameters that were simulated, and these values were chosen based on the behavior of an MH tank.

Following the prediction of these parameters, COMSOL software was used to determine charge and discharge rates vs time to reach 90% of the maximum hydrogen capacity. The charging rate for hydrogen in an MH tank was obtained to be 2.7 kg/m^3s . A discharge rate graph versus time to attain 90% of the maximum hydrogen capacity, was computed using COMSOL software. Based on this number, it can be concluded that the charging rate for hydrogen in the metal hydride tank is 2.5kg/m^3s, which means 0.2 kg/m^3s was lost inside the MH due to some of the energy being lost and converted to heat.

REFERENCES

AFZAL, M. & SHARMA, P. 2018. Design of a large-scale metal hydride-based hydrogen storage reactor: Simulation and heat transfer optimization. *International Journal of Hydrogen Energy,* 43**,** 13356-13372.

BAO, Z., YANG, F., WU, Z., CAO, X. & ZHANG, Z. 2013. Simulation studies on heat and mass transfer in high-temperature magnesium hydride reactors. *Applied Energy,* 112**,** 1181-1189.

BILL REHM, D. 2012. Situational Problems in MPD. *Managed Pressure Drilling.*

BIROL, F. 2019. The Future of Hydrogen.

BUSQUE, R., TORRES, R., GRAU, J., RODA, V. & AND HUSAR, A. 2017. Effect of metal hydride properties in hydrogen absorption through 2D-axisymmetric modeling and experimental testing in storage canisters. *Hydrogen energy,* 44**,** 19114-19125.

CAMARA, R. T. & ATTILA, P. H. 2015. Metal hydride state of charge estimator Universitat Politècnica de Catalunya Institut de Robòtica i Informàtica Industrial

JIAO, K., LI, X., YIN, Y., ZHOU, Y., YU, S. & DU, Q. 2012. Effects of various operating conditions on the hydrogen absorption processes in a metal hydride tank. *Applied Energy,* 94**,** 257-269.

LOTOTSKYY, M. & LINKOV, V. 2022. Thermally driven hydrogen compression using metal hydrides. *International Journal of Energy Research,* 46**,** 22049-22069.

LOTOTSKYY, M., SATYA SEKHAR, B., MUTHUKUMAR, P., LINKOV, V. & POLLET, B. G. 2015. Niche applications of metal hydrides and related thermal management issues. *Journal of Alloys and Compounds,* 645**,** S117-S122.

MELLOULI, S., ASKRI, F., DHAOU, H., JEMNI, A. & BEN NASRALLAH, S. 2010. Numerical simulation of heat and mass transfer in metal hydride hydrogen storage tanks for fuel cell vehicles. *International Journal of Hydrogen Energy,* 35**,** 1693-1705.

NICHOLS, L. 2020. *Connecting Gas Properties to Kinetic Theory of Gases* [Online]. Available: https://chem.libretexts.org/Bookshelves/Physical and Theoretical Chemistry Textbook Maps/Supplemental Modules (Physical and Theoretical Chemistry)/Physical Properties of Matter/States of Matter/Properties of Gases/Kinetic Theory of Gases/Connecting Gas Properties to Kinetic Theory of Gases [Accessed 11 November 2022].

OLDENBURG, U. 2016. Viscosity and Reynolds Numbers. *Institute of Physics Module Introductory Laboratory Course Physics – Part I.* Carl von Ossietzky University Oldenburg.

SATYA SEKHAR, B., LOTOTSKYY, M., KOLESNIKOV, A., MOROPENG, M. L., TARASOV, B. P. & POLLET, B. G. 2015. Performance analysis of cylindrical metal hydride beds with various heat exchange options. *Journal of Alloys and Compounds,* 645**,** S89-S95.

SHAHRZAD, S. M., GRAY, E. M. & WEBB, C. J. 2016. A review of mathematical modelling of metal-hydride systems for hydrogen storage applications. *International Journal of Hydrogen Energy,* 41**,** 3470-3484.

ZHANG, S.-Z., ZHAO, L. & HE, J.-H. 2015. A modified Stanton number for heat transfer through the fabric surface. *Thermal Science,* 19**,** 1475-1477.

Bongiwe Ladyfair Hem

Process engineer in Training
Tshwane university of Technology

Bongiwe Ladyfair Hem is a dynamic and results-driven process engineer in training, passionate about innovation, sustainability, and strategic problem-solving in industrial operations. Currently with Idwala Industrial Holdings, as a process engineer in training where she specializes in process optimization, energy efficiency, and the implementation of eco-friendly solutions in mining and chemical engineering. She is a registered Candidate Engineer with the Engineering Council of South Africa (ECSA) and an Associate Member of the Southern African Institute of Mining and Metallurgy (SAIMM).

Bongiwe holds a Master of Engineering (MEng) in Chemical Engineering from Tshwane University of Technology, where her research focused on optimization of hydrogen storage using COMSOL modelling software. Additionally, she explored simulation and problem-solving using AnyLogic, integrating system dynamics, discrete event modelling, and agent-based approaches to develop dynamic business models that enhance operational efficiency and sustainability in industrial processes.

Her professional experience spans industrial operations, research, and academia. She has worked on diverse projects, including process optimization in mining operations, water and wastewater treatment, and the integration of sustainable practices. As a researcher at the Council for Scientific and Industrial Research (CSIR), she was involved in forward osmosis, reverse osmosis, and membrane distillation technologies to treat acid mine drainage and brine, contributing to water conservation and resource recovery initiatives.

In her current role, Bongiwe is responsible for monitoring plant processes, conducting energy and material balance analyses, and supporting the implementation of process modifications and technology trials to enhance efficiency. She actively collaborates with cross-functional teams, ensuring compliance with environmental regulations and safety standards while driving continuous improvement in operational performance.

Beyond her technical expertise, Bongiwe has a strong academic background, having spent over two years mentoring and supervising chemical engineering students. She has experience in practical training, tutoring, and guiding students through experimental work and industry-related projects. This has strengthened her leadership skills and ability to communicate complex engineering concepts effectively.

Bongiwe is eager to further develop her expertise in sustainable mining practices, hydrogen technologies, and energy transition strategies to contribute to a greener future. She aims to bridge the gap between research and industry by applying innovative solutions to real-world challenges in mining and process engineering.

Her unique blend of technical expertise, research-based perspectives, and strategic leadership positions her as a significant force in promoting sustainable industrial practices. She is still dedicated to using teamwork, creativity, and lifelong learning to create significant change as she pursues her engineering career.

Investigation of Pt ternary alloy catalysts as PEMFC ORR catalysts

Z. Mseleku, T. Ngwenya, K. Tshehla, C. Gray

Mintek, South Africa

The slow kinetics of the cathodic oxygen reduction reaction (ORR) poses a challenge in the industrialisation of PEMFCs. Additionally, high Pt content is required to overcome the large overpotential of the ORR, resulting in high cost of the catalysts required. To mitigate this, the Pt content can be reduced while improving the ORR activity by alloying Pt with transition metals, which results in a downshift of the Pt d-band and weakens the Pt-O bond. This work investigated synthesising Pt ternary alloy catalysts with low Pt content and testing the activity towards ORR. Pt- M_1-M_2/C catalysts with a Pt content of 20 wt% (where M_1 and M_2 are combinations of Co, Cu and Ni) were synthesised via an aqueous deposition chemical reduction method. Characterisation via XRD analysis showed that the Pt alloy crystallite size was between 3 and 5 nm, which concurs with the theoretical Pt desorption crystallite size from TF-RDE measurements. A slight shift of the XRD peaks to higher 2θ values indicated successful alloying of Pt with base metals. The preliminary TF-RDE results showed a slight improvement in the ORR activity and stability of the Pt ternary alloy catalysts compared to the commercial Platalite-K40 (Pt/C) catalyst.

INTRODUCTION

Proton exchange membrane fuel cells (PEMFCs) have been recognised as a crucial technology in low-carbon energy conversion, due to their high efficiency and lesser environmental impact compared to traditional combustion engines (Ren *et al.*, 2019). Simply put, hydrogen fuel cells produce energy by electrochemically converting hydrogen to protons which recombine with oxygen to produce electricity and water as a byproduct. However, the widespread adoption of PEMFC technology in industry has been hindered by the sluggish kinetics of the cathodic oxygen reduction reaction (ORR) and the cost of the platinum (Pt) which is primarily used as the catalyst in these systems (Ren *et al.*, 2019; B. Hu *et al.*, 2021). PEMFCs are highly dependent on platinum-based catalysts because of their superior activity and durability compared to other noble metals (Wang *et al.*, 2018; Ren *et al.*, 2019). Despite their effectiveness, Pt-based catalysts still do not give the optimal power density and attempts to increase the Pt loading may lead to agglomeration of the Pt nanoparticles which reduces the electrochemical active surface area (ECSA) (Kriston *et al.*, 2013) and thus the activity of the catalyst.

In response to the demand of cost-effective alternatives, researchers have studied various strategies to reduce the catalyst cost whilst maintaining or increasing the performance of the Pt-based catalysts. A promising approach is the synthesis of Pt-ternary alloys by alloying Pt with non-noble transition metals such as cobalt (Co), nickel (Ni), and copper (Cu) (Kriston *et al.*, 2023; Lokanathan *et al.*, 2018; B. Hu *et al.*, 2021). The enhancement of the ORR activity is accredited to the intrinsic electronic effect generated during the alloying process, as a result of the downshift of the Pt d-band centre, culminating in adjustments of the binding energy between Pt and oxygen intermediates formed during the ORR (Hu *et al.*, 2017; Tian *et al.*, 2019; B. Hu *et al.*, 2021). Recently, de-alloyed Pt bimetallic nanoparticles gained a lot of attention, where a Pt-rich skin is formed in a core-shell framework. These studies indicated a significant enhancement in catalytic efficacy pertaining to the ORR (Mani, Srivastava and Strasser, 2011; Heggen *et al.*, 2012; Zhang *et al.*, 2015; Strasser and Kühl, 2016; Xiao *et al.*, 2021).

Considering the above- mentioned studies, using two transition metals combined with Pt has been suggested as a promising option to optimise electrocatalytic performance in PEMFCs even further (Zhang *et al.*, 2015; Strasser and Kühl, 2016; Xiao *et al.*, 2021). As a result, Bin *et al.,2021* synthesised PtCuCo/C which exhibited a mass activity, three-fold that of commercial Pt/C (B. Hu *et al.*, 2021). Zhang *et al.,2023* successfully used a polyol method and thermal annealing to prepare CoNi-Pt/C-600, which showed superior electrocatalytic performance to Johnson Matthey (JM) Pt/C (Zhang *et al.*, 2023).

Various methods have been previously employed to synthesise the alloys, such as wet chemical synthesis (Zhang *et al.*, 2021), chemical reduction (Fu *et al.*, 2016), laser irradiation (Hu *et al.*, 2023), and co- deposition (Muntean *et al.*, 2020). For instance, Bin Hu and co-workers used a novel co-doping strategy for the large-scale synthesis of Pt–Cu–Co ternary alloy catalysts for PEMFCs. The co-doping of Cu and Co optimises the electronic structure of Pt, enhancing the activity for the ORR. The synthesised PtCuCo catalyst showed superior mass activity compared to commercial Pt/C catalysts. Furthermore, the catalyst exhibits good durability, with only a small decrease of 9.5% in activity after 30,000 cycles (Fu *et al.*, 2016). Inasmuch as the methods stated above are yielding catalysts with a promising ORR activity, the amount of Pt in these catalysts is significantly high, above 30 %wt. Secondly it is not viable to upscale using most of the methods due to the cost of the equipment required. As a result, a different synthesis and easily scalable approach is needed, hence the aqueous deposition chemical reduction method developed at Mintek was used in this project.

The main aim of this paper was to enhance the ORR activity of Pt catalysts while lowering the Pt weight percentage (wt%). This was done by alloying Pt with non-noble transition metals of Co, Ni and Cu. The Pt-based ternary alloys were prepared using a modified aqueous deposition chemical reduction method, followed by the alloying process at high temperatures (500-900°C). After the synthesis of the ternary alloy catalysts, a thorough characterisation was conducted using various analytical techniques such as X-ray diffraction (XRD) and high-resolution transmission electron microscopy (HRTEM) for structural analysis, followed by assessment of their electrochemical performance and stability using TF-RDE (thin-film rotating disk electrode) measurements. The success of this study has the potential to lower the total cost of PEMFCs by reducing the amount Pt used as catalyst whilst also improving the sluggish ORR activity.

Experimental section

Preparation of ternary alloys

Three ternary alloy catalysts were synthesised utilising an aqueous deposition chemical reduction technique. Generally, this method involves dissolution of metal precursors into metal ions like Cu2+ from copper nitrate in a water-based solution while stirring. A suitable reducing agent must be added into the solution which acts as an electron donor to the metal ions to reduce them to their metal state; this is followed by the aggregation of metal atoms to form nanoparticles. These nanoparticles are then dispersed onto the surface of high surface area carbon material to form a catalyst. The summarised standard method with modifications which are proprietary to Mintek was used, followed by alloying process. In each of the three catalysts, a metal loading of 22 wt% was targeted, comprising 20 wt% Pt and 2 wt% of the additional two transition metals. The employed synthesis methodology represents a variant of wet chemistry and heat treatment processes, which guarantees an optimal dispersion of metallic nanoparticles across the surface of the carbon support. The alloying process was conducted by placing each catalyst in a stationery tube furnace at temperatures ranging between 500 - 900 ^{o}C under 5% H_2/N_2 gas for two hours. The alloyed catalysts were collected and de-alloyed by washing in acidic solution to remove excess base metals. After de-alloying, the dried catalysts powder was placed back into the furnace under the same gas mixture but at lower temperatures (Þ400^{o}C) for annealing. This process closes the pores on the alloy core-shell structure that were opened during the de-alloying step.

Scientific and Industrial Research (CSIR). The metal weight (%) loading was determined by ashing each catalyst at 700^{o}C for three hours.

Electrochemical characterisation

All electrochemical measurements were executed at a controlled temperature of 25°C in a conventional three-electrode cell. Pt foil functioned as the counter electrode, a saturated calomel electrode (SCE) was used as the reference electrode, and a glassy carbon rotating disk electrode (RDE) was employed as the working electrode. The rotation speed and the potential of the working electrode were regulated by an Autolab PGSTAT302N potentiostat, utilising NOVA v1.11 software. Prior to conducting the measurements, the preparation of the catalyst ink involved weighing ±20 mg of the catalyst into a glass vial, followed by the addition of a calculated volume of high-purity water per gram of Pt, after which the mixture was sonicated for a duration of 20 minutes at ambient temperature. A volume of 20 µl of the prepared ink was subsequently dropped onto the surface of the glassy carbon electrode using a micro-pipette and allowed to dry for 30 minutes. Following this, 20 µl of a 5% Nafion solution was dripped onto the 5 mm diameter glassy carbon electrode surface and dried in an oven at 120°C for 10 minutes. A commercially available Platalite-K40 (Pt/C) catalyst, was utilised as a benchmark to facilitate the comparison of the electrochemical characteristics of the advanced catalysts. Cyclic voltammetry was conducted within the potential range of 0.05 to 1.25 V (versus RHE) at sweep rates of 50 and 20 mV/s in a nitrogen-purged 0.1 M $HClO_4$ solution, while accelerated durability tests (ADT) were executed between 0.60 and 1.00 V (versus RHE) at a scan rate of 20 mV/s over 7200 cycles in accordance with the Nissan ADT Procedure (Takahashi and Kocha, 2010). The evaluation of the oxygen reduction reaction (ORR) was carried out through linear sweep voltammetry (LSV) from 0.12 to 1.02 V (vs RHE) at a scan rate of 20 mV/s in an oxygen-saturated 0.1 M $HClO_4$ solution.

Results and discussion

Structural characterization

Before TF-RDE measurements, XRD was employed to characterise structural differences of the crystallites for each catalyst crystal structure differences of each catalyst. Displayed in Figure 1 is the XRD patterns of the various ternary alloy catalysts with each sample exhibiting four peaks characteristic of the metal face-centred cubic (fcc) structure. A broad diffraction peak which is found at $2\theta \approx 46^{o}$ is attributed to Pt (111) plane. This diffraction peak shifts to a higher angle (47.748^{o}, 47.958^{o}, 47.790^{o}) for alloy catalysts compared to that of Pt only catalyst (46.625^{o}). The observed shift can be attributed to lattice contraction which confirms alloying of metals (Seo *et al.*, 2006). The diffraction peak shift for the ternary alloy catalysts was observed not only for the Pt (111) peak but also for all other peaks; Pt (200), Pt (211), and Pt (311) as can be seen in Figure 1. The XRD lattice parameter calculations from Pt (111) peak were recorded in Table I to acquire the detailed information of the lattice constants. Based on the diffraction angle analysis of Pt/C, PtCoNi/C, PtCoCu/C and PtCuNi/C, there is a more notable shift in the peaks for PtCoCu/C than other catalysts, indicating a stronger lattice compression. The compressive Pt lattice strain occurs due to the interaction between Pt and metal atoms with a smaller radius like Co, Ni and Cu, and becomes stronger as more atoms are bonded (Luo *et al.*, 2019). The compressive strain positively affects the ORR by lowering the binding energy between Pt and ORR intermediate species such as O^{*}, $OH^{\cdot}$ and $OOH^{\cdot}$. This effect occurs because compressive strain causes a broadening of the d-band on the Pt-surface (B. Hu *et al.*, 2021).

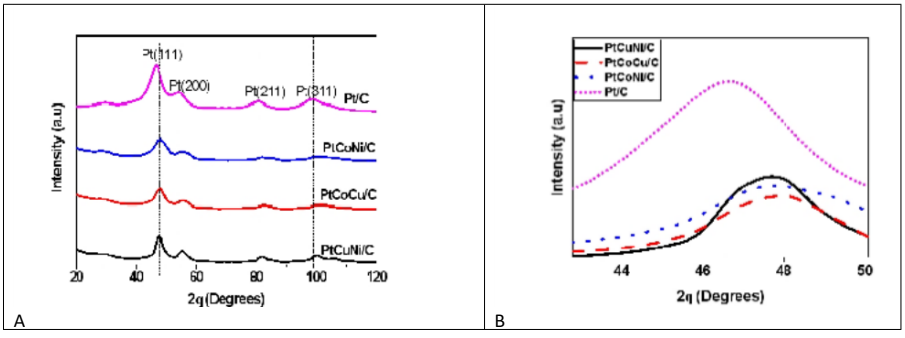

Figure 1. (A) XRD patterns of ternary alloys catalysts: PtCoNi/C, PtCoCu/C, PtCuNi/C and Pt/C. (B) Magnification of Pt (111) peak.

Table II. XRD results of Pt/C and alloy catalysts

Catalyst	Pt (111) Peak Position (2θ)	Lattice Parameter (Å)	Crystallite size (nm)
Pt/C	46.625	3.915	2.70
PtCoNi/C	47.748	3.828	3.79
PtCoCu/C	47.958	3.812	3.88
PtCuNi/C	47.790	3.825	4.60

HRTEM analysis

Particle size and distribution was studied using HRTEM. The results obtained from HRTEM analysis of the synthesised ternary alloys were analysed for particle size distribution and the results are presented in a graphic form in Figure 2. It was observed that the metal particles were uniformly dispersed on the surface of the carbon support as can be seen in the Figure 2 images. This indicates that metal alloy particles were successfully dispersed on the surface of the carbon support during synthesis. The analysis of the average particle size of PtCuCo/C, PtCuNi/C and PtCoNi/C showed that PtCuCo/C has the smallest particles at 2.36 nm followed by PtCoNi/C at 3.02 nm and PtCuNi/C at 3.03 nm. The smaller particle size is an indication of a good catalyst because particle size plays an important role in catalytic activity. Smaller particles turn out to have a larger surface area-to-volume ratio, which increases the number of active sites available for the reaction (Gilliam *et al.*, 2011).

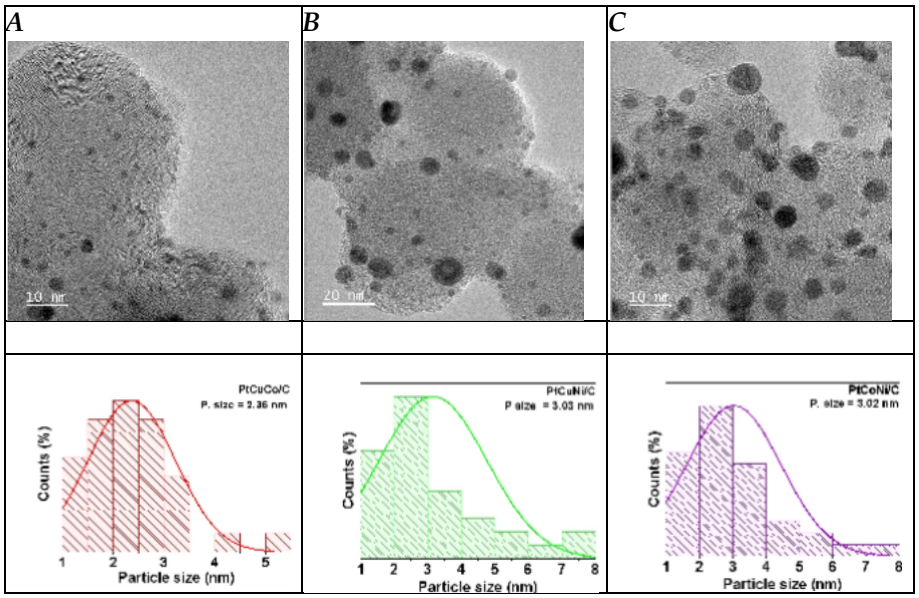

Figure 2. HRTEM images of the synthesised ternary alloys and a graphical illustration of particle size distribution.

Electrochemical characterisation

Electrochemical tests were conducted in a three-electrode system to evaluate the ORR activity of the various catalysts. These tests involved measuring the mass activity (MA) and specific activity (SA) of ternary alloys in an oxygen-saturated 0.1 M perchloric acid ($HClO_4$) solution. Figure 3(A-D) summarises catalyst ECSA (Figure 3A), MA and SA (Figure 3B), ECSA% loss after durability test (Figure 3C) and catalyst cyclic voltammograms (Figure 3D). The results, displayed in a bar graph in Figure B, indicate that the ternary alloys exhibited higher MA and SA compared to the commercial Pt/C catalyst. Specifically, the PtCoNi/C and PtCoCu/C alloys achieved the highest mass activities of 0.21 A/mg_{Pt}, which is approximately 1.3 times the mass activity of the Pt/C catalyst (0.17 A/mg_{Pt}). In terms of specific activity, the PtCuNi/C alloy produced the highest at 351±40 $\mu A/cm^2_{Pt}$, which is 2.5 times that

of the Pt/C catalyst (139±3 μA/cm$^2_{Pt}$). The electrochemical active surface area (ECSA) of the catalysts were measured using the hydrogen underpotential deposition (Hupd) as shown in Figure 2 (D). The ECSA values for PtCoNi/C, PtCoCu/C, and PtCuNi/C were found to be 98±9, 70±1, and 54±2 m^2/g.$_{Pt}$, respectively. These values were lower than that of the Pt/C catalyst (118±3 m^2/g.$_{Pt}$), which was as a result of the lower Pt loading of the alloyed catalysts, at 20 wt%, whilst Platalite®-K40 (Pt/C) had a 40 wt% loading (Y. Hu *et al.*, 2021). Durability tests for all the synthesised catalysts were conducted for 7200 potential cycles as reported in Figure (C). All of the ternary alloys showed improved stability compared to Pt/C (65% ECSA remaining), PtCuNi/C exhibited a superior stability of 93% ECSA remaining after 7200 potential cycles. PtCoNi/C and PtCoCo/C maintained 76% and 77% ECSA after 7200 potential cycles, respectively. An unexpected increase in the ECSA of PtCuNi/C was observed during the ADT run, this can be attributed to the fact that PtCuNi/C had excess base metals covering the Pt surface, these base metals may dissolve during the multiple potential cycling of the durability test, leaving Pt-rich layer resulting in more Pt active cites, giving a temporal increased ECSA (Xiao *et al.*, 2021; Đukić *et al.*, 2022).

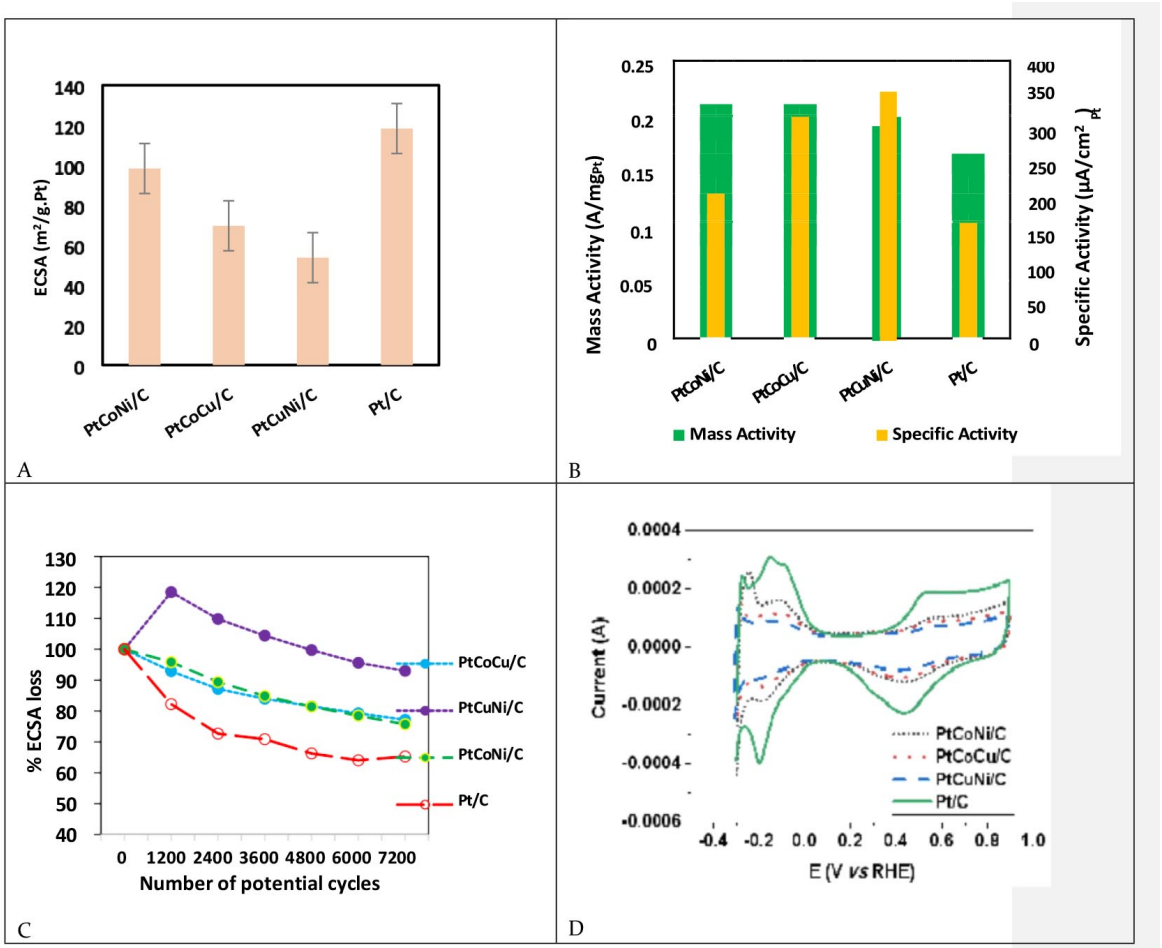

Figure 3. (A) bar graph plot for the electrochemical active surface area of the catalysts (B) a comparison of mass and specific activity for all the catalysts, (C) % ECSA remaining during the durability test and (D) cyclic voltammograms of all catalysts.

CONCLUSION

Pt-based ternary alloy catalysts, PtCoNi/C, PtCoCu/C and PtCuNi/C were synthesised successfully. These ternary alloys displayed improved ORR performance in acidic solutions. The analysis of XRD data confirmed the successful alloying of Pt, Co, Ni and Cu metals in the catalysts. From electrochemical testing it is concluded that the average SA and MA values of the catalyst were 2.2 and 1.3 times larger than that of Pt/C, respectively. In addition, after the durability testing, the ECSA of Pt/C significantly decreased, whereas the ternary alloys maintained relatively stable ECSA. These findings clearly demonstrate that ternary alloys outperform the commercially available Pt/C catalyst. This study demonstrates the capability to produce ternary alloy catalysts with enhanced ORR activity and stability by adjusting the electronic and crystal structures of the catalyst nanoparticles. It offers a dependable method for advancing the development of catalysts while lowering the total cost of PEMFC catalysts by reducing Pt content. Future projects will focus on upscaling the ternary alloys to a larger synthesis scale whilst optimising the synthesis method to obtain even better ORR activity performance. For future recommendations more studies will be conducted to determine a precise alloying temperature for best performance and the ternary alloy catalysts will be characterised in-situ as a single cell MEA.

REFERENCES

Đukić, T., Pavko, L., Jovanovič, P., Maselj, N., Gatalo, M., & Hodnik, N. (2022). Stability challenges of carbon-supported Pt-nanoalloys as fuel cell oxygen reduction reaction electrocatalysts. Chemical Communications, 58(100), 13832–13854. https://doi.org/10.1039/D2CC05377B

Fu, S., Zhu, C., Song, J., Engelhard, M. H., Xia, H., Du, D., & Lin, Y. (2016). Kinetically Controlled Synthesis of Pt-Based One-Dimensional Hierarchically Porous Nanostructures with Large Mesopores as Highly Efficient ORR Catalysts. ACS Applied Materials and Interfaces, 8(51), 35213–35218. https://doi.org/10.1021/ACSAMI.6B11537/SUPPL_FILE/AM6B11537_SI_001.PDF

Gilliam, R. J., Kirk, D. W., & Thorpe, S. J. (2011). Influence of Structural, Microstructural and Electrical Properties on Electrocatalytic Performance at the Nanoscale. Electrocatalysis, 2(1), 1–19. https://doi.org/10.1007/s12678-011-0038-1

Heggen, M., Oezaslan, M., Houben, L., & Strasser, P. (2012). Formation and analysis of core-shell fine structures in Pt bimetallic nanoparticle fuel cell electrocatalysts. Journal of Physical Chemistry C, 116(36), 19073–19083. https://doi.org/10.1021/jp306426a

Hu, B., Yuan, J., Zhang, J., Shu, Q., Guan, D., Yang, G., Zhou, W., & Shao, Z. (2021). High activity and durability of a Pt–Cu–Co ternary alloy electrocatalyst and its large-scale preparation for practical proton exchange membrane fuel cells. Composites Part B: Engineering, 222. https://doi.org/10.1016/j.compositesb.2021.109082

Hu, S., Cheng, K., Ribeiro, E. L., Park, K., Khomami, B., & Mukherjee, D. (2017). A facile and surfactant-free route for nanomanufacturing of tailored ternary nanoalloys as superior oxygen reduction reaction electrocatalysts. Catalysis Science and Technology, 7(10), 2074–2086. https://doi.org/10.1039/C7CY00073A

Hu, T., Fan, Y., Ye, Y., Cai, Y., Liu, J., Ma, Y., Li, P., & Liang, C. (2023). Laser Irradiation-Induced Pt-Based Bimetallic Alloy Nanostructures without Chemical Reducing Agents for Hydrogen Evolution Reaction. Catalysts, 13(6), 1018. https://doi.org/10.3390/CATAL13061018/S1

Hu, Y., Zhu, M., Luo, X., Wu, G., Chao, T., Qu, Y., Zhou, F., Sun, R., Han, X., Li, H., Jiang, B., Wu, Y., & Hong, X. (2021). Coplanar Pt/C Nanomeshes with Ultrastable Oxygen Reduction Performance in Fuel Cells. Angewandte Chemie International Edition, 60(12), 6533–6538. https://doi.org/10.1002/ANIE.202014857

Kriston, A., Xie, T., Ganesan, P., & Popov, B. N. (2013). Analysis of the effect of Pt Loading on Mass and Specific Activity in PEM Fuel Cells.

Lokanathan, M., Patil, I. M., Navaneethan, M., Parey, V., Thapa, R., & Kakade, B. (2018). Designing of stable and highly efficient ordered Pt2CoNi ternary alloy electrocatalyst: The origin of dioxygen reduction activity. Nano Energy, 43, 219–227. https://doi.org/10.1016/j.nanoen.2017.11.041

Luo, B., Zhao, F., Xie, Z., Yuan, Q., Yang, F., Yang, X., Li, C., & Zhou, Z. (2019). Polyhedron-Assembled Ternary PtCuCo Nanochains: Integrated Functions Enhance the Electrocatalytic Performance of Methanol Oxidation at Elevated Temperature. ACS Applied Materials and Interfaces, 11(35), 32282–32290. https://doi.org/10.1021/ACSAMI.9B10192/SUPPL_FILE/AM9B10192_SI_001.PDF

Mani, P., Srivastava, R., & Strasser, P. (2011). Dealloyed binary PtM3 (M = Cu, Co, Ni) and ternary PtNi3M (M = Cu, Co, Fe, Cr) electrocatalysts for the oxygen reduction reaction: Performance in polymer electrolyte membrane fuel cells. Journal of Power Sources, 196(2), 666–673. https://doi.org/10.1016/J.JPOWSOUR.2010.07.047

Muntean, R., Pascal, D. T., Rost, U., Mărginean, G., Brodmann, M., & Vaszilcsin, N. (2020). Synthesis and characterisation of platinum–cobalt–manganese ternary alloy catalysts supported on carbon nanofibers: An alternative catalyst for hydrogen evolution reaction. International Journal of Hydrogen Energy, 45(49), 26217–26225. https://doi.org/10.1016/J.IJHYDENE.2020.02.041

Ren, X., Lv, Q., Liu, L., Liu, B., Wang, Y., Liu, A., & Wu, G. (2019). Current progress of Pt and Pt-based electrocatalysts used for fuel cells. Sustainable Energy & Fuels, 4(1), 15–30. https://doi.org/10.1039/C9SE00460B

Seo, A., Lee, J., Han, K., & Kim, H. (2006). Performance and stability of Pt-based ternary alloy catalysts for PEMFC. Electrochimica Acta, 52(4), 1603–1611. https://doi.org/10.1016/j.electacta.2006.03.097

Strasser, P., & Kühl, S. (2016). Dealloyed Pt-based Core-Shell Oxygen Reduction Electrocatalysts.

Takahashi, I., & Kocha, S. S. (2010). Examination of the activity and durability of PEMFC catalysts in liquid electrolytes. Journal of Power Sources, 195(19), 6312–6322. https://doi.org/10.1016/j.jpowsour.2010.04.052

Tian, X., Zhao, X., Su, Y. Q., Wang, L., Wang, H., Dang, D., Chi, B., Liu, H., Hensen, E. J. M., Lou, X. W., & Xia, B. Y. (2019). Engineering bunched Pt-Ni alloy nanocages for efficient oxygen reduction in practical fuel cells. Science, 366(6467), 850–856. https://doi.org/10.1126/SCIENCE.AAW7493

Wang, Y. J., Long, W., Wang, L., Yuan, R., Ignaszak, A., Fang, B., & Wilkinson, D. P. (2018). Unlocking the door to highly active ORR catalysts for PEMFC applications: polyhedron-engineered Pt-based nanocrystals. Energy & Environmental Science, 11(2), 258–275. https://doi.org/10.1039/C7EE02444D

Xiao, Z., Jiang, Y., Wu, H., Zhong, H., Song, H., Abdelhafiz, A., & Zeng, J. (2021). De-alloyed ternary electrocatalysts with high activity and stability for oxygen reduction reaction. Journal of Alloys and Compounds, 877. https://doi.org/10.1016/j.jallcom.2021.160221

Zhang, B., Wu, J., & Cong, Y. (2023). PtCoNi Alloy Towards Efficient Oxygen Reduction Reaction. E3S Web of Conferences, 441. https://doi.org/10.1051/E3SCONF/202344101022

Zhang, P., Dai, X., Zhang, X., Chen, Z., Yang, Y., Sun, H., Wang, X., Wang, H., Wang, M., Su, H., Li, D., Li, X., & Qin, Y. (2015). One-Pot Synthesis of Ternary Pt-Ni-Cu Nanocrystals with High Catalytic Performance. Chemistry of Materials, 27(18), 6402–6410. https://doi.org/10.1021/ACS.CHEMMATER.5B02575/SUPPL_FILE/CM5B02575_SI_001.PDF

Zhang, X., Li, H., Yang, J., Lei, Y., Wang, C., Wang, J., Tang, Y., & Mao, Z. (2021). Recent advances in Pt-based electrocatalysts for PEMFCs. RSC Advances, 11(22), 13316–13328. https://doi.org/10.1039/D0RA05468B

Synthesis, characterisation and testing of ruthenium-modified iridium oxide ($IrxRuyO_2$) catalyst in a laboratory scale proton exchange membrane water electrolysers (PEMWE)

D. Zide[1,2], A. Sinto[1,2], S. Chidziva[2], T. Oosthuysen[1], T. Tawonezvi[1,2], S. Pasupathi[2], B.J. Bladergroen[2]

[1]Cape Peninsula University of Technology, South Africa
[2]University of the Western Cape, South Africa

The development of highly stable and efficient catalysts for proton exchange membrane water electrolyzers (PEMWE) is crucial for advancing the oxygen evolution reaction (OER). IrO_2 is a widely used catalyst due to its stability; however, its high cost necessitates the exploration of alternative or modified materials to improve cost-effectiveness. This study successfully synthesized Ru-modified IrO_2 and unsupported IrO_2 via the Adams Fusion Method. The synthesized catalysts were characterized using XRD and SEM to analyze their elemental composition, crystal structure, and morphology. Electrochemical performance was evaluated through CV, LSV, and chronoamperometry (CA) to assess OER activity and durability. Furthermore, the study assessed the membrane electrode assembly (MEA) performance of synthesized $Ir_{0.7}Ru_{0.3}O_2$ electrocatalysts for PEMWE. The $Ir_{0.7}Ru_{0.3}O_2$ catalyst exhibited superior catalytic activity compared to commercial IrO_2, suggesting that incorporating Ru enhances OER performance while reducing catalyst costs. Additionally, the in-house catalyst-coated membranes outperformed commercial alternatives, highlighting their potential for PEM electrolyzers. The $Ir_{0.7}Ru_{0.3}O_2$ demonstrated excellent electrochemical performance, offering a cost-effective alternative for green hydrogen production. MEA testing confirmed that synthesized $Ir_{0.7}Ru_{0.3}O_2$ outperformed commercial catalysts in terms of current density and overall efficiency, highlighting its potential for sustainable hydrogen production.

Keywords: Electrocatalysis; Oxygen evolution reaction (OER); Proton exchange membrane water electrolyzers (PEMWE); Iridium oxide-based catalystIntroduction

INTRODUCTION

The global energy landscape is undergoing a significant transformation due to increasing energy demands. Currently, fossil fuels account for approximately 80% of the global energy mix, while renewables contribute about 20%(Gielen et al., 2019). The extensive use of fossil fuels has a detrimental impact on the environment, primarily due to carbon dioxide (CO_2) emissions, which is a major driver of climate change. Research indicates that fossil fuel reserves could be depleted within 50-60 years, necessitating a rapid transition to renewable energy sources (Wang and Azam, 2024).

One of the challenges associated with renewable energy is the high cost of PEMWE technology. Expensive materials, particularly the proton exchange membrane water electrolysers (PEMWE) anode catalyst, hinder the widespread adoption of clean hydrogen production. In addition, the oxygen evolution reaction (OER) is among the major limiting factor in PEMWE due to its high energy requirements and slower kinetics compared to the hydrogen evolution reaction (HER) (Gouws and Mackay, 2024). The performance of OER primarily depends on the catalyst used, with platinum group metals (PGMs) being the most commonly employed due to their superior activity.

To achieve efficient and sustainable hydrogen production, it is essential to develop catalysts that accelerate chemical reactions in PEMWE. Due to the acidic environment of Nafion, noble metal catalysts are required (Chen *et al.*, 2021). Ir-based catalysts are preferred due to their high activity and durability; however, their scarcity and cost necessitate the development of alternatives that maintain catalytic performance while reducing metal loading.

Given the high cost of Ir-based materials, several strategies have been proposed to enhance their Ru performance while reducing cost. One approach involves doping IrO_2 with inexpensive metals to improve catalytic activity and stability. RuO_2 is the most active catalyst for OER; it is however, not RuO_2. Another strategy is to support the catalyst on a high-surface-area material(Polonský et al., 2012, which reduces agglomeration and increases the active surface area (Karimi and Peppley, 2017). An ideal OER catalyst support should exhibit excellent stability under harsh OER conditions, good electrical conductivity, and low cost. Additionally, (Karimi and Peppley, 2017) that an effective support material should enhance catalyst activity and durability by modifying its electronic structure. Transition metal carbides have gained interest as potential support materials (Karimi and Peppley, 2017).

Various synthesis methods can be employed for IrO_2-based catalysts, including electrochemical synthesis, hydrothermal methods, sol-gel processes, and precursor thermal decomposition (Ahmed and Mao, 2016). However, many of these techniques are complex, expensive, environmentally hazardous, and rely on unstable precursors. These drawbacks, which pose both economic and technical challenges, include the need for sophisticated experimental setups and time-consuming synthesis procedures (Karels et al. 2024).The modified Adams fusion method (MAFM) was selected for this study due to its simplicity, stability, and cost-effectiveness. MAFM has been demonstrated to directly produce nanosized metal oxides with high efficiency (Felix *et al.*, 2019)

MATERIALS AND METHODS

Material

The synthesis of ruthenium-modified iridium oxide (Ru-modified IrO_2) required iridium chloride ($IrCl_3$), isopropanol (99.9%), ruthenium chloride ($RuCl_3$), and sodium nitrate ($NaNO_3$), all of which were sourced from Alfa-Aesar, United States. For the preparation of the working electrodes, Nafion Solution (5%) and commercial iridium oxide (IrO_2) were also obtained from Alfa-Aesar, while ruthenium-modified iridium oxide ($RuIrO_2$) was synthesised in-house. Additionally, ultra-pure water (Milli-Q) was prepared in-house to ensure high purity in the electrode fabrication process.

Catalyst Synthesis

The unmodified IrO_2 was synthesised by dissolving $IrCl_3 \cdot xH_2O$ in isopropanol. The solution was magnetically stirred for 30 minutes at 300 rotations per minute (rpm). Finely ground $NaNO_3$ was added to the mixture and stirred for another 30 min. The isopropanol was then evaporated from the mixture on a hotplate and dried in an oven for 15 min at 85℃. The dried mixture was cooled and transferred to a porcelain crucible. The synthesis duration was constant at two hours while the temperature was 350°C. The obtained metal oxide was filtered four times with 500 mL of Milli-Q ultrapure H_2O to remove the unreacted salts. A 0.1M $AgNO_3$ solution was used to ensure no chloride was present in the last 500 mL ultrapure water filter filtrate. In the final step, the $RuIrO_2$ was dried at 85℃ for two hours and cooled inside the oven overnight and stirred. Finely crushed $NaNO_3$ was added, followed by heating to remove solvents. The dried mixture was calcined at 350°C for two hours, cooled overnight, and rinsed with ultrapure water before drying.

Ru-modified IrO_2 was synthesised by dissolving iridium chloride ($IrCl_3 \cdot xH_2O$) and ruthenium chloride ($RuCl_3$) separately in isopropanol to make individual precursor solutions. The iridium and ruthenium precursor solutions were then combined and magnetically stirred for 30 min at 300 rotations per minute (rpm). The process followed the same drying, calcination, cooling, and rinsing steps as for unmodified IrO_2 synthesis.

Physical Characterisation
The crystalline structure was then analysed using X-ray diffraction (XRD), Bruker AXS XRD instrument. Measurements were operated in a continuous θ - θ scan in locked coupled mode with Cu-Kα radiation (λKα1=1.5406Å) in the 2-theta range from 5° to 70°, in steps of 0.034° per second. The morphology, and surface texture of individual particles and the elemental composition of the anode catalyst samples were analysed by means of high-resolution scanning electron microscopy (HR-SEM), Phenom pro instrument; samples were prepared by dispersing a representative portion of each catalyst samples onto double-sided carbon tape mounted on a SEM stub.

Electrochemical Investigation
A glassy carbon electrode was polished, ultrasonicated, and dried to prepare the working electrode. Catalyst ink was prepared by dispersing a pre-weighed amount of the catalyst in ultrapure water and Nafion, with 8 mg deposited onto the electrode and dried. Electrochemical analysis was conducted using a three-electrode setup (glassy carbon working electrode, 3 M of Ag/AgCl reference electrode, and Pt sheet counter electrode 1 $cm^{2)}$ was used. The electrolyte (0.5 M H_2SO_4) was degassed with nitrogen. CV, LSV, and CA measurements were performed using an Autolab potentiostat, with a potential window of 0 to +1.4 V versus RHE applied at a scan rate of 20 mV/s for 50 cycles prior to any electrochemical characterisations, and for LSV and CP analyses, the RDE speed was set to 1600 rpm

Catalyst Ink preparation (Anode and Cathode)
For the anode catalyst loading of 2.5 mg/cm^2 of iridium oxide (IrO_2) or ruthenium-modified iridium oxide on a 25 cm^2 Nafion membrane, the required metal loading was calculated and weighed-out. $_2$. The catalyst ink was prepared using a 1:6:2 ratio of the pre-weighed of IrO_2 or ruthenium-modified iridium oxide catalyst, Nafion solution 5% w/w so and solvent, respectively. To account for potential material loss during preparation, an additional 10% of the total mass was included, with all components adjusted proportionally. Isopropanol was used as the dispersion medium, and the mixture was homogenised by sonication for 30 minutes to ensure uniform dispersion of the catalyst. For the cathode to achieve a platinum on carbon (Pt/C) loading of 0.5 mg/cm^2 on a 25 cm^2 Nafion membrane, the required platinum on carbon was calculated as 31.25 mg. The same procedure as for the anode was followed for the preparation of the cathode ink, maintaining consistency in the preparation method.

Deposition method
The proton exchange membrane (PEM) was placed into a metal frame and clamped with a binder clip on all sides for equal distribution of pressure; this was clamped to a piece of clapboard to reduce the amount of warping when spraying the catalyst ink onto the membrane, as warping in the presence of isopropanol lowers the performance of the MEA. In the fume hood, the catalyst ink was sprayed with a spray gun (nozzle calibre: 0.3 mm) using nitrogen gas to pressurise the spray gun. The process of spraying the catalyst took place under an infrared light to evaporate the solvent. Figure 1 illustrates the fabrication process of MEA, from raw material to cell test.

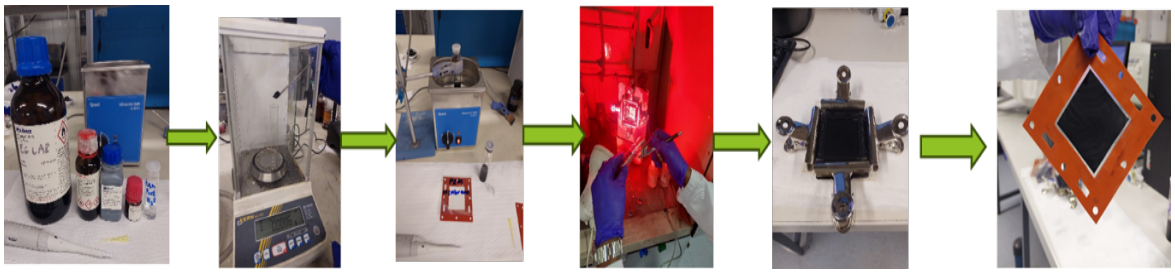

Figure 1. The membrane electrode assembly fabrication steps.

In-house and Commercial MEA Fabrication
Figure 2 demonstrates the gaskets' design. MEA consists of CCM sandwiched between silicon rubber gaskets with a thickness of 210 micrometers. The gasket is needed to create a seal, preventing the leakage of water and gas produced on the electrolysis. The three-step manufacturing process consisted of (i) Soft

rubber gasket printing using a Vicsign vinyl cutter. (ii) Align and impose the CCM in between two gaskets. (iii) The gaskets and CCM are heat-pressed together.

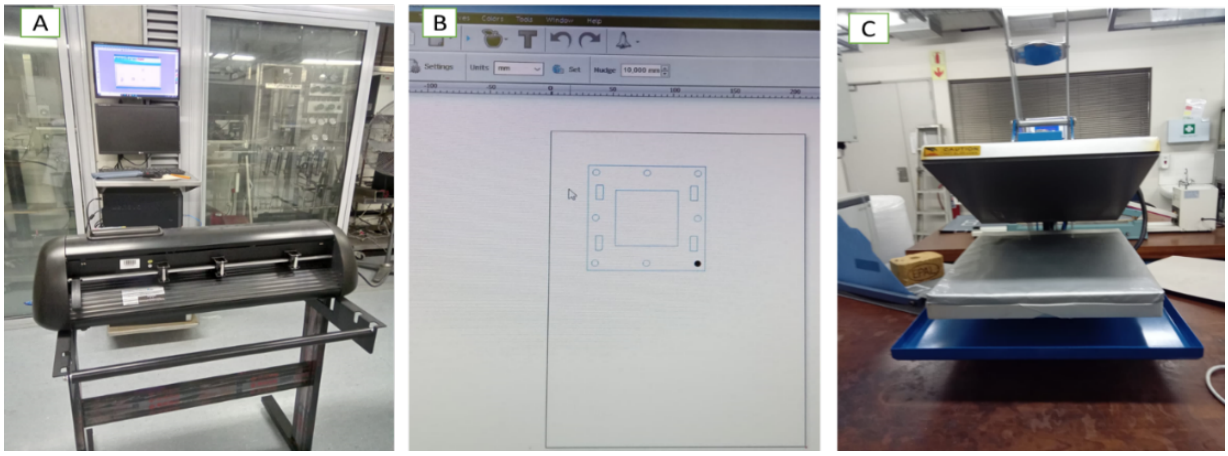

Figure 2. Vicsign HCL630 vinyl cutter setup with the SignMaster 3.5 CUT software. (B) Screenshot of the SignMaster 3.5 Cut software with the gasket design displayed. (C) RoHS HFS (40x50mm) heat press machine.

Membrane Electrode Assembly (MEA) Testing Using an AutoLab Potentiostat

A PEMWE single cell with an active area of 5 cm × 5 cm was used to evaluate the performance of an in-house MEA coated with commercial IrO_2 and in-house CCM coated with synthesised $Ir_{0.7}Ru_{0.3}O_2$ on the anode side.

RESULTS AND DISCUSSION

Physical Characterisation

The XRD spectra of commercial IrO_2, synthesised IrO_2, commercial RuO_2, and synthesised $Ir_{0.7}Ru_{0.3}O_2$ are shown in Figure 3. The peaks were assigned using standard IrO_2 data from the XRD analysis software. Figure 3A and C illustrate the XRD patterns of commercial IrO_2 and commercial RuO_2, respectively. The peaks of these two commercial samples appear at the same diffraction angles, indicating similar crystalline structures. However, the peak intensities of RuO_2 are notably higher than those of IrO_2, suggesting a higher degree of crystallinity. The narrow peaks observed in both commercial catalysts confirm their crystalline nature. In contrast, the XRD patterns of synthesised IrO_2 and synthesised $Ir_{0.7}Ru_{0.3}O_2$ (Figure 3B and D) exhibit broader peaks, indicating their amorphous nature. The key diffraction peaks for both commercial catalysts appear at approximately 29°, 35°, 40°, and 54°as per the data standard, also corresponding with those reported in literature (Felix, 2019) and (Kareis, *et al.*, 2024).

Figure 4 compares the XRD patterns of all samples, showing that the peak positions of the synthesised catalysts closely match those of their commercial counterparts.

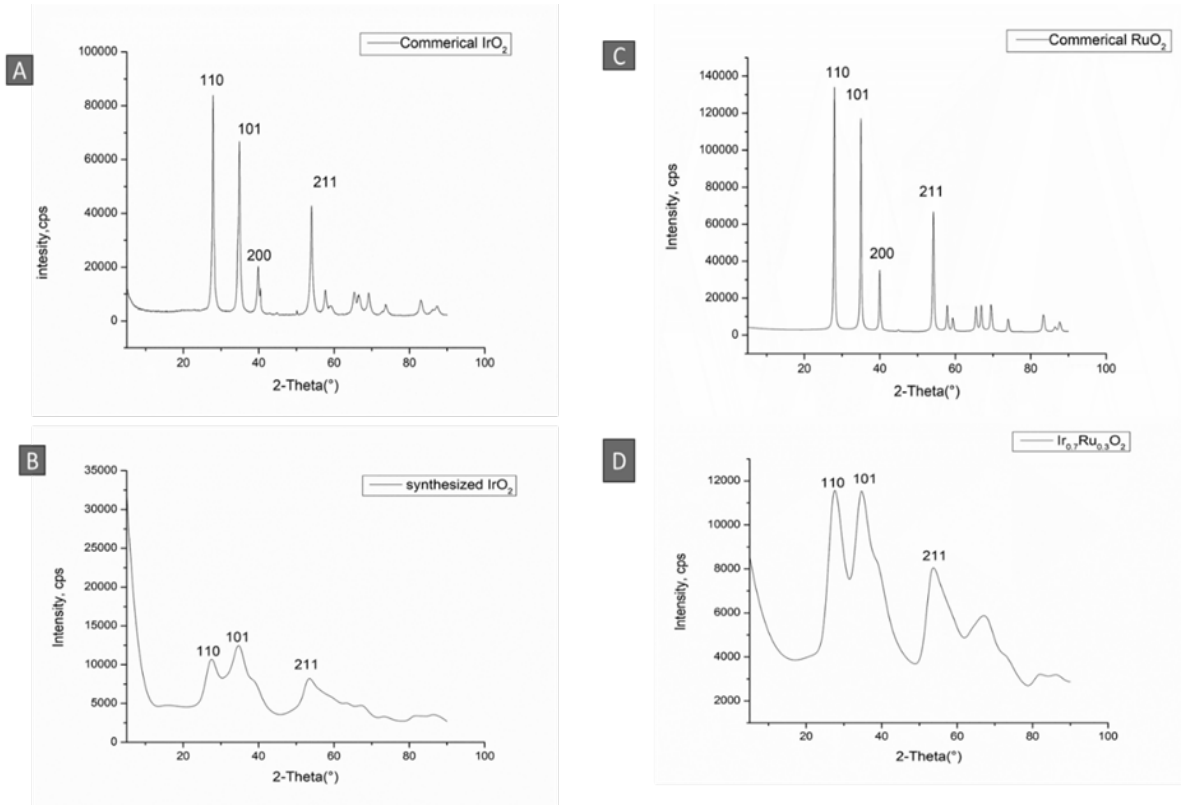

Figure 3. XRD pattern for four electrocatalysts - (A) Commercial IrO_2, (B) Synthesised IrO_2, (C) Commercial RuO_2, (D) Synthesised $Ir_{0.7}Ru_{0.3}O_2$.

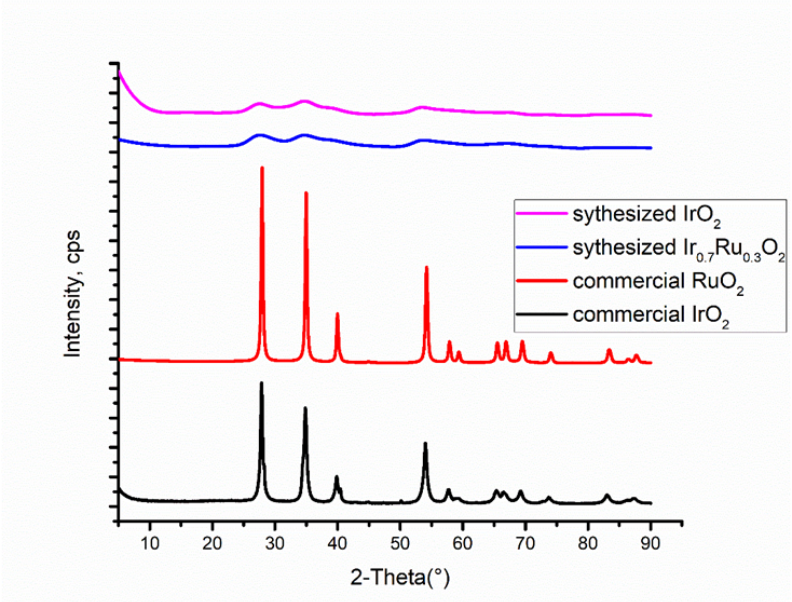

Figure 4. XRD pattern comparison of commercial and synthesised electrocatalysts.

The SEM images of commercial IrO_2, synthesised IrO_2, commercial RuO_2, and synthesised $Ir_{0.7}Ru_{0.3}O_2$ are presented in Figure 5. The results reveal that synthesised IrO_2 exhibits non-uniformly distributed agglomerated crystals.

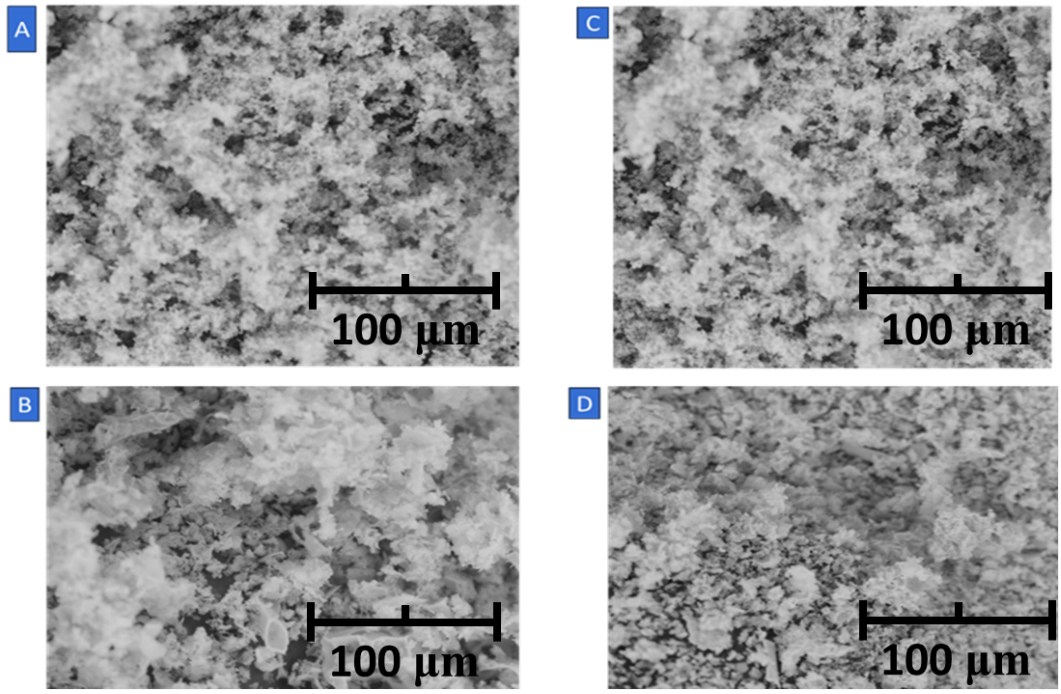

Figure 5. SEM images of electrocatalysts - (A) Commercial IrO_2, (B) Synthesised IrO_2, (C) Commercial RuO_2, (D) Synthesised $Ir_{0.7}Ru_{0.3}O_2$.

The amorphous nature of synthesised IrO_2, as indicated by the broader XRD peaks (Figure 5B), corresponds to its less-defined crystal morphology. Conversely, the well-defined crystalline nature of commercial IrO_2 aligns with its sharp XRD peaks (Figure 5A). The higher surface area of commercial IrO_2, due to reduced agglomeration, likely contributes to its superior electrocatalytic performance compared to the synthesised sample (Kareis, *et al.*, 2024). Similarly, the SEM image of synthesised $Ir_{0.7}Ru_{0.3}O_2$ reveals agglomerated crystals with a non-uniform distribution, indicating a lower surface area compared to commercial IrO_2 and RuO_2. The broad peaks in its XRD pattern (Figure 5D) further confirm its amorphous nature. The lower surface area and increased aggregation in synthesised $Ir_{0.7}Ru_{0.3}O_2$ could lead to reduced electrocatalytic performance due to fewer exposed active sites. Additional characterisation via transmission electron microscopy (TEM) would be beneficial to determine crystal size more precisely.

Electrochemical Characterisation

Cyclic voltammetry (CV) was conducted to evaluate the redox behaviour and electrochemical properties of the four electrocatalysts. Figure 6 presents the cyclic voltammograms of commercial IrO_2, synthesised IrO_2, commercial RuO_2, and synthesised $Ir_{0.7}Ru_{0.3}O_2$. The CV analysis of commercial IrO_2 (Figure 6A) shows distinct oxidation and reduction peaks, attributed to the redox transitions of Ir species. The first redox couple at ~0.4 V corresponds to $Ir^{III/IV}$ (Ox1/Red1), while the second redox couple at ~0.8 V is associated with $Ir^{IV/V}$ (Ox2/Red2) (Rivera *et al.*, 2013). These peaks confirm the electrocatalytic activity of IrO_2 for the oxygen evolution reaction (OER).

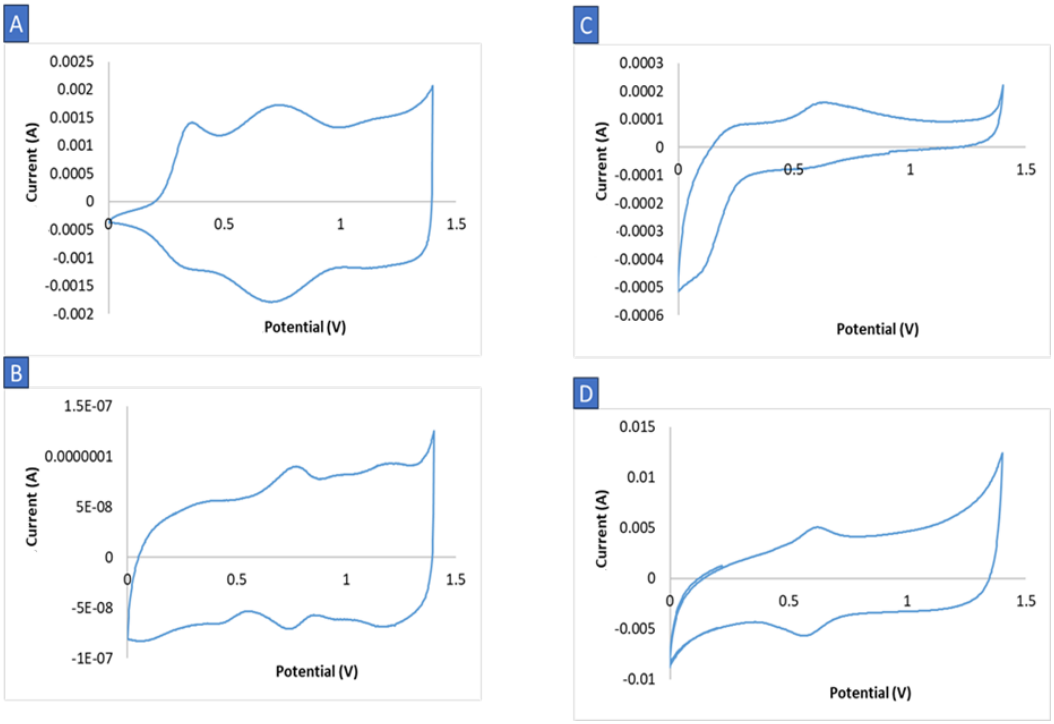

Figure 6. Cyclic voltammogram of four electrocatalysts. (A) Commercial iridium oxide. (B) Synthesised iridium oxide (C) Commercial ruthenium oxide. (D) Synthesised ruthenium modified iridium oxide.

The CV of synthesised IrO_2 (Figure 6B) exhibits similar redox transitions but with lower current densities. In Figure 6C, the oxidation and reduction peaks of commercial RuO_2 are less pronounced, with a small peak at ~0.6 V representing Ru(IV) to Ru(III) oxidation and a corresponding reduction peak at ~0.5 V. Figure 6D shows the redox behaviour of synthesised $Ir_{0.7}Ru_{0.3}O_2$, with oxidation occurring at ~0.6 V and reduction at ~0.5 V. The redox potential range closely resembles that of RuO_2, suggesting minimal variation in redox behaviour between these catalysts. However, the higher peak current of synthesised $Ir_{0.7}Ru_{0.3}O_2$ indicates improved electrochemical activity compared to individual IrO_2 and RuO_2 catalysts.

Linear sweep voltammetry (LSV) analysis was performed at a scan rate of 2 mV/s in 0.5 M H_2SO_4 at 25°C and atmospheric pressure, with the RDE speed set to 1600 rpm. Figure 4.5 presents the LSV curves of the electrocatalysts. Among all catalysts, synthesised $Ir_{0.7}Ru_{0.3}O_2$ exhibited the highest activity. Its current density remained stable within the 0.8 -1.47V potential window before increasing exponentially. At 1.6V, synthesised $Ir_{0.7}Ru_{0.3}O_2$ achieved a high current density of 0.4A cm^{-2}, indicating superior electrocatalytic performance in OER.

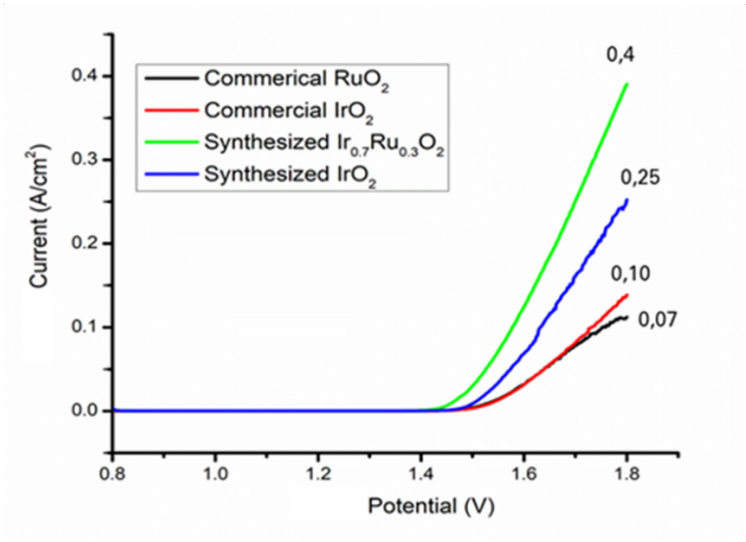

Figure 7. LSV plots of electrocatalysts (commercial IrO_2, commercial RuO_2, synthesised IrO_2 and synthesised $Ir_{0.7}Ru_{0.3}O_2$) at 0.002 V/s.

Chronopotentiometry (ChronoP) analysis was used to evaluate catalyst stability at a current density of 0.01 A/cm². Figure 8 presents the ChronoP results. Synthesised $Ir_{0.7}Ru_{0.3}O_2$ exhibited the longest stability, maintaining a steady potential of ~1.45 V for over seven hours before degradation. Synthesised IrO_2 remained stable at ~1.55 V for the same duration, while commercial IrO_2 and RuO_2 exhibited shorter stability periods of five and four hours, respectively.

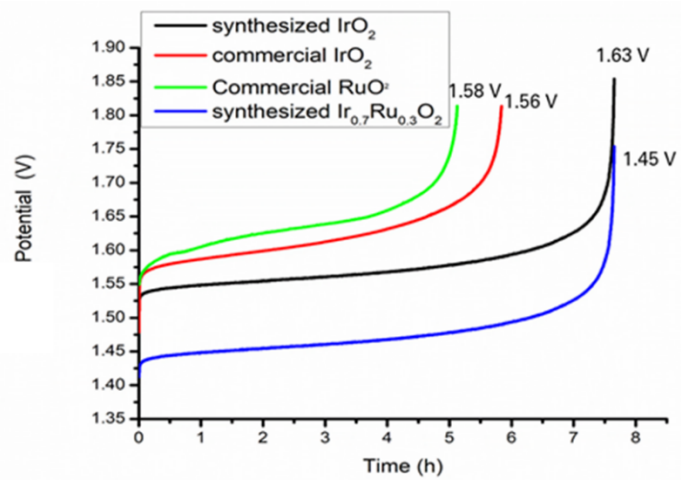

Figure 8. Chronopotentiometric stability of electrocatalysts - chrono of commercial IrO_2, commercial RuO_2, synthesised IrO_2 and synthesised $Ir_{0.7}Ru_{0.3}O_2$.

Membrane electrode assembly testing

The performance of membrane electrode assemblies (MEAs) in PEMWE systems was evaluated using different anode catalysts. The results indicate that MEAs incorporating synthesised $Ir_{0.7}Ru_{0.3}O_2$ exhibited superior performance compared to commercial IrO_2 and RuO_2 (Figure 9). At an applied voltage of 1.8 V, the current density of the synthesised $Ir_{0.7}Ru_{0.3}O_2$-based MEA reached 2.0 A, significantly higher than that of commercial catalysts. This improvement suggests enhanced electrocatalytic activity and proton conductivity, facilitating effective charge transfer and reduced energy consumption.

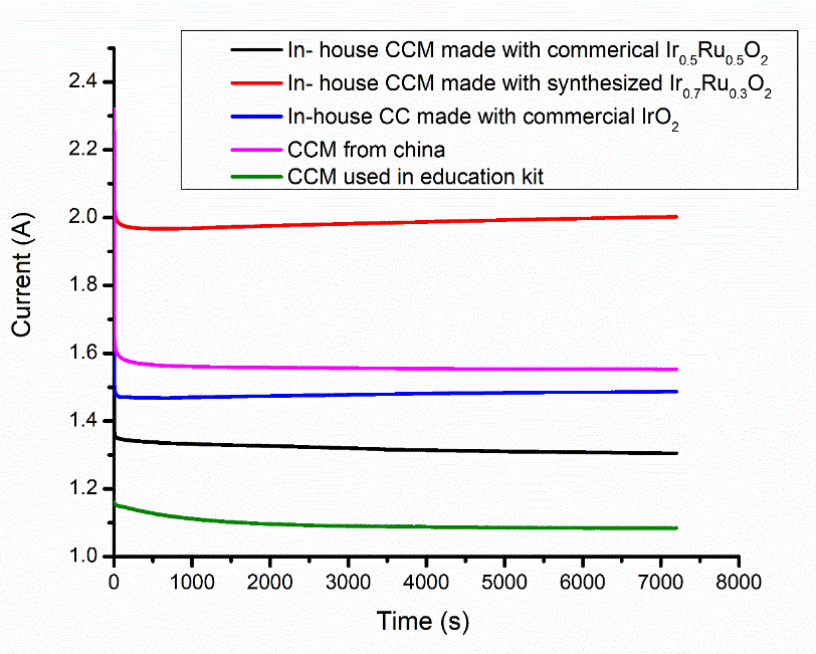

Figure 9. The evaluation performance of CCM coated with different catalysts.

To validate the performance of the fabricated MEAs under real-world conditions, testing was conducted using both a commercial cell-based electrolyser (Figure 10A) and an in-house fabricated proton exchange membrane (PEM) electrolyser system (Figure 10B). The in-house PEM electrolyser featured an active surface area of 25 cm^2 and operated at a temperature of 78°C. Electrochemical performance was assessed at applied voltages of 1.4 V and 1.9 V, with a water flow rate of 25 mL/min. The recorded current output was 5 A at 1.4 V and 3 A at 1.9 V.

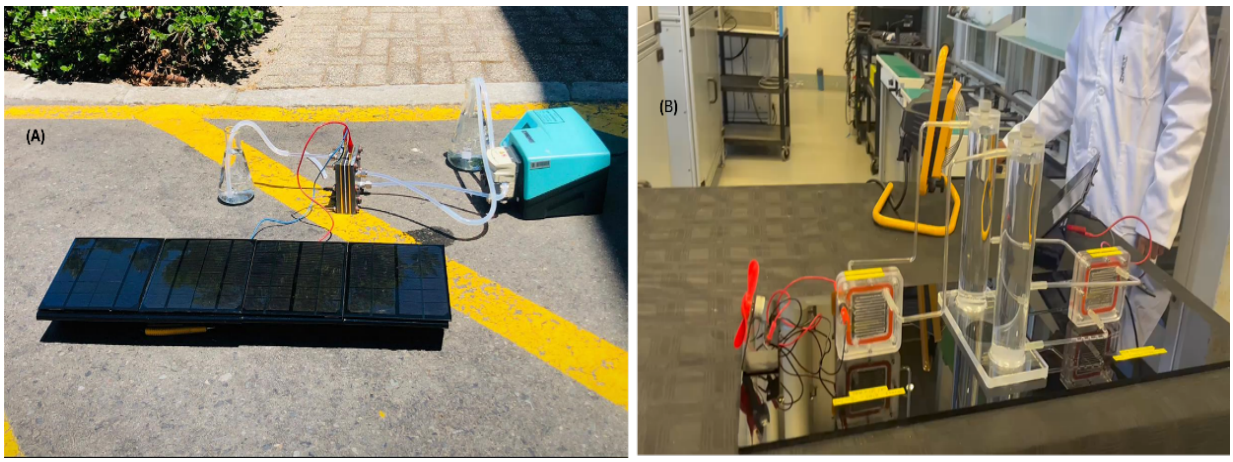

Figure 10. Testing of membrane electrode assembly in real world- (A) The testing was conducted outside using a commercial cell-based electrolyser and (B) The testing was performed inside using an in-house fabricated cell electrolyser system.

The performance trends observed during laboratory scale experiments were consistent with real-world testing, reinforcing the efficiency and applicability of the synthesised $Ir_{0.7}Ru_{0.3}O_2$ catalyst for industrial hydrogen production. The PEM electrolyser cell efficiencies, calculated based on hydrogen low heating value (LHV) and high heating value (HHV), were determined to be 65% and 85%, respectively. Under operational conditions, the cell produced a peak current of 1.73 A at 1.9 V. The power output of the test cell was calculated as 3.287 W and 7 W for both LHV and HHV cases. The total system energy input

was 2.7 V, while the energy output was 2.2 V, resulting in an overall system efficiency of 65% for LHV and 85% for HHV.

Hydrogen Production and Energy Efficiency Analysis:

The hydrogen generation rate was calculated using the equation, **H_2 (kg)= (η x P x t)/E**

Where:

- **η** = Electrolyser efficiency
- **P** = Power input (kW)
- **t** = Time (hours)
- **E** = Energy required to produce 1 kg H_2 (**39.4 kWh/kg**)

Hydrogen Production at LHV Efficiency (65%):

H_2(LHV) = (0.65×0.003287 kW×1 h) / 39.4kWh kg^{-1} = 0.005427091 kg ≈ 5.43 g h^{-1}

Hydrogen Production at HHV Efficiency (85%):

H_2(HHV) = (0.85×0.003287 kW×1 h) / 39.4 kWh kg^{-1} = 0.007091 kg ≈ 7.1 g h^{-1}

The performance data from the test cell (Figure B) was further utilised to develop a demonstration model, which consists of:

- A PEM electrolyser cell
- Hydrogen and oxygen storage towers
- A single-cell PEM fuel cell
- A fan acting as a load

The electrolyser system was powered using solar energy, harvested via solar panels (Figure A), showcasing its potential for renewable-driven hydrogen production. These findings highlight the feasibility of integrating PEM electrolysers into sustainable energy systems while optimising catalyst design to enhance overall efficiency.

CONCLUSION

This study demonstrates the successful synthesis of $Ir_{0.7}Ru_{0.3}O_2$ as an efficient electrocatalyst for PEMWE applications. XRD and SEM analyses confirmed its amorphous structure, while electrochemical testing showed enhanced redox behaviour, higher current densities, and improved stability compared to commercial catalysts. MEA testing validated its efficiency, achieving 65% LHV and 85% HHV efficiencies, with hydrogen production rates of 5.43 g/h (LHV) and 7.1 g/h (HHV). Real-world testing, including a solar-powered electrolyser model, reinforced its potential for sustainable hydrogen production. These findings highlight the feasibility of optimising catalyst design for industrial-scale green hydrogen applications. Thus, further research should explore optimisation strategies to enhance catalyst durability and scalability for industrial applications.

Author Contributions: Conceptualisation, D.Z.; methodology, D.Z., and A.S.; software, D.Z., S.C., and B.J.B.; validation, D.Z.; formal analysis, D.Z., and A.N.; resources, D.Z., S.C., S.P., and B.J.B.; writing - original draft preparation, D.Z.; writing - review and editing, D.Z., A.S., T.T., S.C., B.J.B.; funding

acquisition, S.P., and B.J.B.; supervision, D.Z.; S.C., and B.J.B.; project administration, D.Z. All authors have read and agreed to the published version of the manuscript.

Funding: Funding was provided by the Department of Trade, Industry and Competition of the Republic of South Africa as part of the Technology and Human Resources for Industry Programme (THRIP/19/31/08/2018). Some additional funding was provided by the Department of Science and Innovation through the financial and strategic support received from the South African National Energy Development Institute (SANEDI) and the Energy & Water Sector Education Training Authority (EWSETA) in South Africa.

Institutional Review Board Statement: Not applicable

Informed Consent Statement: Not applicable

Data Availability Statement: Additional data is available from the authors upon request.

Acknowledgments: We would like to express our gratitude to the Department of Science and Innovation for the financial and strategic support received from the South African National Energy Development Institute (SANEDI) and the Energy & Water Sector Education Training Authority (EWSETA) in South Africa which is greatly appreciated. Also, the funding from Technology and Human Resources for Industry Program (THRIP/19/31/08/2018) under the Department of Trade, Industry and Competition of the Republic of South Africa is greatly appreciated. Our special thanks go to students and staff of South Africa Institute of Advanced Material Chemistry at the University of the Western Cape and the Chemistry Department at Cape Peninsula University of Technology for their insightful comments and suggestions, which greatly contributed to improving the quality of this paper. Finally, we are grateful to the anonymous reviewers for their constructive feedback and thoughtful suggestions, which have enhanced the clarity and impact of this manuscript.

Conflicts of Interest: The authors declare that they have no known competing financial interests or personal relationships that could have appeared to influence the work reported in this paper.

REFERENCES

Ahmed, J. and Mao, Y. (2016) 'Ultrafine Iridium Oxide Nanorods Synthesized by Molten Salt Method toward Electrocatalytic Oxygen and Hydrogen Evolution Reactions', *Electrochimica Acta*, 212, pp. 686–693. Available at: https://doi.org/10.1016/j.electacta.2016.06.122.

Chen, F.-Y. *et al.* (2021) 'Stability challenges of electrocatalytic oxygen evolution reaction: From mechanistic understanding to reactor design', *Joule*, 5(7), pp. 1704–1731. Available at: https://doi.org/10.1016/j.joule.2021.05.005.

Felix, C. *et al.* (2019) 'Ex-Situ Electrochemical Characterization of IrO2 Synthesized by a Modified Adams Fusion Method for the Oxygen Evolution Reaction', *Catalysts*, 9(4), p. 318. Available at: https://doi.org/10.3390/catal9040318.

Gielen, D. *et al.* (2019) 'The role of renewable energy in the global energy transformation', *Energy Strategy Reviews*, 24, pp. 38–50. Available at: https://doi.org/10.1016/j.esr.2019.01.006.

Gouws, S. and Mackay, J. (2024) 'Production of green hydrogen through PEM water electrolysis', *Pure and Applied Chemistry*, 96(10), pp. 1383–1401. Available at: https://doi.org/10.1515/pac-2023-1022.

Karels, S., Felix, C. and Pasupathi, S. (2024) 'Development of unsupported IrO2 nano-catalysts for polymer electrolyte membrane water electrolyser applications', *South African Journal of Science*, 120(3/4). Available at: https://doi.org/10.17159/sajs.2024/16026.

Karimi, F. and Peppley, B.A. (2017) 'Metal Carbide and Oxide Supports for Iridium-Based Oxygen Evolution Reaction Electrocatalysts for Polymer-Electrolyte-Membrane Water Electrolysis', *Electrochimica Acta*, 246, pp. 654–670. Available at: https://doi.org/10.1016/j.electacta.2017.06.048.

Polonský, J. *et al.* (2012) 'Tantalum carbide as a novel support material for anode electrocatalysts in polymer electrolyte membrane water electrolysers', *International Journal of Hydrogen Energy*, 37(3), pp. 2173–2181. Available at: https://doi.org/10.1016/j.ijhydene.2011.11.035.

Wang, J. and Azam, W. (2024) 'Natural resource scarcity, fossil fuel energy consumption, and total greenhouse gas emissions in top emitting countries', *Geoscience Frontiers*, 15(2), p. 101757. Available at: https://doi.org/10.1016/j.gsf.2023.101757.

Dorcas Zide

Lecturer/ Affiliated Researcher at SAIAMC-UWC
Cape Peninsula University of Technology

Dr. Dorcas Zide is an Analytical Chemist with a strong background in both academia and industry. She earned her PhD from the Cape Peninsula University of Technology (CPUT) in collaboration with the South African Institute for Advanced Materials Chemistry (SAIAMC) at the University of the Western Cape (UWC). Currently a Lecturer at CPUT, she plays a vital role in educating and mentoring future scientists, having previously served as a Chemistry Facilitator and Retention Officer. She is also an Affiliated Researcher at SAIAMC.

Dr. Zide's career extends beyond academia, with significant contributions to industry initiatives. She has worked with PPC Cement, Wesgro, and the Transfer and Industrial Linkages Office (TTO), where she engaged in technology transfer and industrial partnerships. Her expertise spans sustainable energy technologies, including NiFe and Li-ion battery production, membrane capacitive deionization (MCDI), zeolites, nanomaterials, and applied catalysis.

A passionate advocate for sustainability and innovation, Dr. Zide leads research projects tackling environmental challenges. She supervises MSc and PhD students, as well as Work Integrated Learners (WILs), guiding them in critical research areas such as water desalination, green hydrogen production, and electronic waste management - particularly recycling valuable metals from used Li-ion batteries. Her dedication to mentorship was highlighted in 2023 when two of her WIL students secured 1st and 3rd place at the CPUT Chemistry Mini-Symposium Science Idols competition on November 22.

Beyond research and teaching, Dr. Zide actively contributes to international collaborations. She voluntarily serves as the Climate, Energy, and Mobility South African Assistant National Contact Point (ANCP) for the Horizon Europe Framework under the Department of Science and Innovation (DSI). In this role, she facilitates scientific cooperation between South Africa and European researchers. Additionally, she is a trainer for the Green Hydrogen Power to X Training for Decision Makers Workshops, a program led by UWC and the Deutsche Gesellschaft für Internationale Zusammenarbeit (GIZ) GmbH, aimed at promoting the adoption of green hydrogen technologies.